



HAL
open science

Behaviour of a joint between a U-shaped steel-concrete beam and a concrete-filled steel tubular column

P. Heng, C. Lepourry, H Somja, F. Palas

► **To cite this version:**

P. Heng, C. Lepourry, H Somja, F. Palas. Behaviour of a joint between a U-shaped steel-concrete beam and a concrete-filled steel tubular column. *Journal of Constructional Steel Research*, 2020, 175, pp.106322. 10.1016/j.jcsr.2020.106322 . hal-02960421

HAL Id: hal-02960421

<https://hal.science/hal-02960421>

Submitted on 7 Jan 2021

HAL is a multi-disciplinary open access archive for the deposit and dissemination of scientific research documents, whether they are published or not. The documents may come from teaching and research institutions in France or abroad, or from public or private research centers.

L'archive ouverte pluridisciplinaire **HAL**, est destinée au dépôt et à la diffusion de documents scientifiques de niveau recherche, publiés ou non, émanant des établissements d'enseignement et de recherche français ou étrangers, des laboratoires publics ou privés.

Behaviour of a Joint between a U-shaped Steel-Concrete Beam and a Concrete-Filled Steel Tubular Column

Piseth Heng^{a,b,*}, Clemence Lepourry^{a,b}, Hugues Somja^a, Franck Palas^c

^a *Université Européenne de Bretagne - INSA de Rennes, LGCGM/Structural Engineering Research Group, 20 avenue des Buttes de Coësmes, CS 70839, F-35708 Rennes Cedex 7, France*

^b *INGENOVA, Civil Engineering Office, 5 Rue Louis Jacques Daguerre, 35136 Saint-Jacques-de-la-Lande, France*

^c *Concept Technique Design R & D, 89 Boulevard de laval, 35500 Vitré France*

Abstract

A new type of U-shaped steel-concrete beams (USCB) using L-angle shear connectors was recently proposed as an alternative solution for long-span structures. In a specific portal frame configuration used in a recent building, the USCB is connected to concrete-filled steel tubular columns by welded steel-concrete joints. The behaviour of these joints plays a crucial role in the global structural stability of the frame as much as that of the whole building. Due to the composite steel-concrete action within the joint, its design is not explicit nor available in design provisions. This paper has the objective to investigate the behaviour of this complex joint and propose a design model of the joint for practical engineers. An experimental campaign of two full-scale tests was carried out in order to determine the moment resisting capacity, the deformation capacity, the cracking patterns, and the failure mode of the joint. A finite element model of the test was also developed and validated against the experimental results to investigate more closely the load transfer mechanism and the propagation of plastification in the components of the joint. The stress map obtained from the FE model was afterwards used to define the geometry of the design model of the joint. This model was proposed based on the strut-and-tie method for the concrete part and the shear panel model for the steel part of the joint. The interesting feature of the design model is the inclusion of the load transfer mechanism of the forces between the steel and the concrete parts of the joint. Finally, a parametric study on the influence of steel detailing inside the joint using the FE model was carried out. It was found out that the initial solution can be simplified and optimized.

Keywords : Strut-and-tie model; beam-to-column composite joint; U-shaped steel-concrete beams; full-scale experimental tests; FE simulation; shear panel model.

30 1. Introduction

31 Over the past years, different types of composite beams such as an I-profile steel concrete beam
32 [1, 2, 3, 4, 5, 6, 7], an encased I-profile composite beam [8, 9, 10, 11], a steel sheet-concrete beam [12,
33 13], and a U-shaped steel-concrete beam [14, 15, 16, 17] have been proposed in order to achieve the
34 challenging architectural demand for long-span structures such as bridges and commercial buildings.
35 In a previous investigation by the authors [17, 18], a new configuration of a U-shaped steel-concrete
36 beam (USCB) with L-shaped shear connectors was studied. The L-shaped connectors, welded to
37 upper flanges of the U-shaped steel beam, also serves as a bracing to maintain the shape of the
38 steel cross-section during concrete encasement. In a specific frame configuration [18], the USCB
39 is connected to concrete-filled steel tubular columns by composite beam-to-column joints. The
40 behaviour of these complex joints plays a crucial role in the global structural stability of the frame
41 as much as that of the whole building.

42 Conventional beam-to-column joints can be designed following the current norms ([19] for con-
43 crete, [20] for steel, and [21] for composite) and the design provisions such as [22]. For typical
44 configurations of the joint, current design practices however rely largely on the judgement and
45 experience of individual designers, using existing knowledge of reinforced concrete and structural
46 steel joint design [23]. The traditional separation between structural steel and reinforced concrete
47 design as well as the resulting lack of design guidelines have drawn back from the use of composite
48 beam-to-column joints [24]. Further investigations of the joint have been carried out on different
49 configurations in order to provide design recommendations to practitioners. For example, Aziz-
50 inamimi et al [23] developed a design of though beam connection for high strength concrete infilled
51 circular or pipe composite column. Their design method was based on the load-transfer mecha-
52 nism, in which the portion of the steel tube between the beam flanges acts as a stiffener, resulting
53 in a concrete compression strut which assists the beam web within the joint in carrying shear. Fur-
54 thermore, Taoa et al [25] investigated the behaviour of composite joints consisting of concrete-filled
55 steel tubular columns, steel beams and through-bolt connections by performing ten experimental
56 tests. Fan et al [26] made six tests on the specimens of 3D joints between concrete-filled square
57 steel tubular columns and composite steel-concrete beams taking into account the effect of concrete

*Corresponding author.

Email address: piseth.heng@insa-rennes.fr (Piseth Heng)

58 slab. On the other hand, Park et al [27] performed two experimental tests on full-scale specimens
59 of a joint between concrete-filled U-shaped steel beam and RC column to verify the seismic per-
60 formance of the connection. Hwang et al [28] carried out three full-scale tests on beam-column
61 connection of pre-fabricated steel-reinforced concrete angle columns and concrete-filled U-shaped
62 steel beams, and proposed a calculation method. In their method, the joint shear strength was
63 contributed by three elements: web shear yielding, direct strut action of the infilled concrete inside
64 the U-section, and strut-and-tie action between the concrete outside of the U-section and the band
65 plate. However, load-transfer mechanism between the elements was not provided. To the knowl-
66 edge of the authors, the behaviour of the joint between the concrete-infilled tubular steel columns
67 and the U-shaped steel-concrete beams has not been studied yet in the literature.

68 This paper investigates the mechanical behaviour of the particularly complex configuration of
69 the composite joint between the CFST column and the novel U-shaped steel-concrete beam. The
70 main objective of the study is the development of a design method of this joint for design engineers.
71 The use of strut-and-tie model for traditional beam-to-column concrete joint is usually straight-
72 forward. However, the extension of the strut-and-tie model in composite joints, particularly the
73 complex configuration of the current joint in this paper, is not trivial and requires an experimental
74 validation. Two full-scale experimental tests are performed on the joint specimens in order to de-
75 termine the moment resisting capacity, the deformation capacity, the damage and cracking pattern,
76 and the failure mode of the joint. To gain more insights on the force transfer mechanism between
77 the components within the joint, a finite element model is also developed in ABAQUS/Explicit [29]
78 and validated against the experimental results. Based on the stress pattern obtained from the FE
79 model, a design model is proposed with a detailed design procedure by adopting the conventional
80 joint models described in Eurocodes (the strut-and-tie model [19] and the shear panel model [20])
81 integrated with the load-transfer mechanism. One of the main features of the design model is the
82 inclusion of the load transfer mechanism of the forces between the steel and the concrete parts of
83 the joint. The model is also able to apply the know-how engineering models, i. e. strut-and-tie
84 model and shear panel model, providing a simple design tool for the practical engineers. Although
85 the model is developed for a particular configuration of the joint, the development of the design
86 model in this paper provides a clear example of the definition of the stress/strain patterns as well
87 as the load-transfer mechanism from the beam to the column and between the steel and concrete

88 parts of the joint. This development could be readily used to adapt to other configurations of
89 beam-to-column composite joints.

90 2. Experimental program

91 2.1. Test setup

92 The size of the specimens is chosen to represent the edge part of the frame, which consists of
93 a CFST column and a hogging part of the USCB (see [18]). As illustrated in Figs. 1 and 2, the
94 test setup consists of a specimen of the joint, a force jack with a capacity of 1500 kN, and a rigid
supporting system. Rotated by 90° , the specimen is pinned at the end of the column and at the

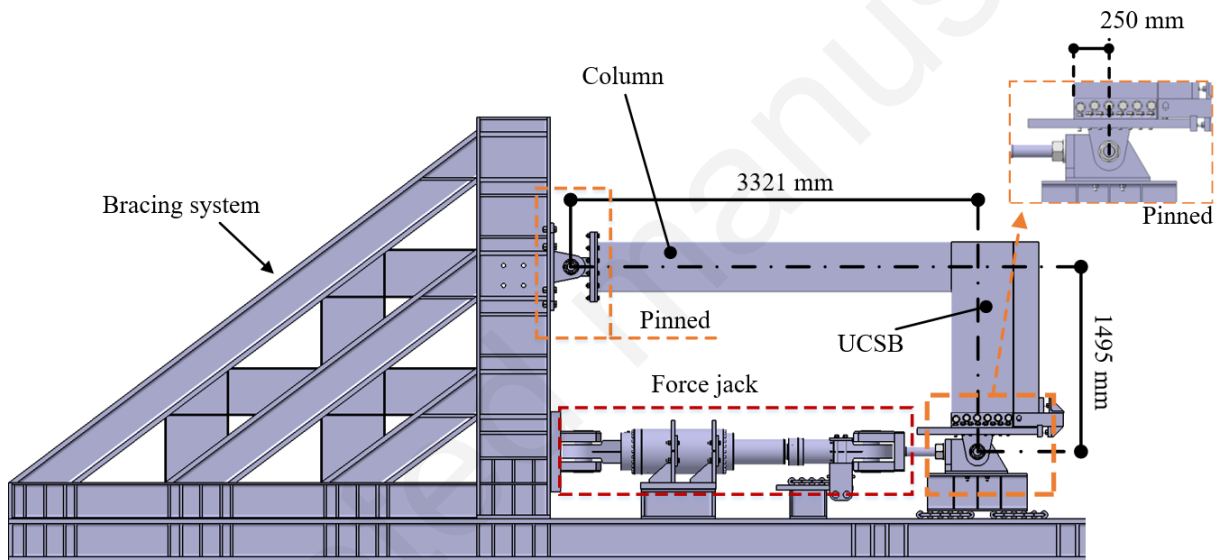


Figure 1: Test setup.

95
96 end of the beam. The position of the pin at the end of the beam matches with the location of the
97 inflection point of the bending moment diagram in the actual frame.

98 Fixed against the rigid reacting wall that serves as a horizontal and vertical support to the
99 specimen, the pin at the bottom of the column allows the transferring of normal and shear forces
100 while keeping zero bending moment (see Fig. 3). The force jack imposes a horizontal displacement
101 to the pin at the beam edge, corresponding to an applied shear force and a zero bending moment.
102 These boundary conditions result in a bending moment in the specimen that is similar to the one
103 of the actual frame (Fig. 3). To ensure the good distribution of the load on the U-shaped profile

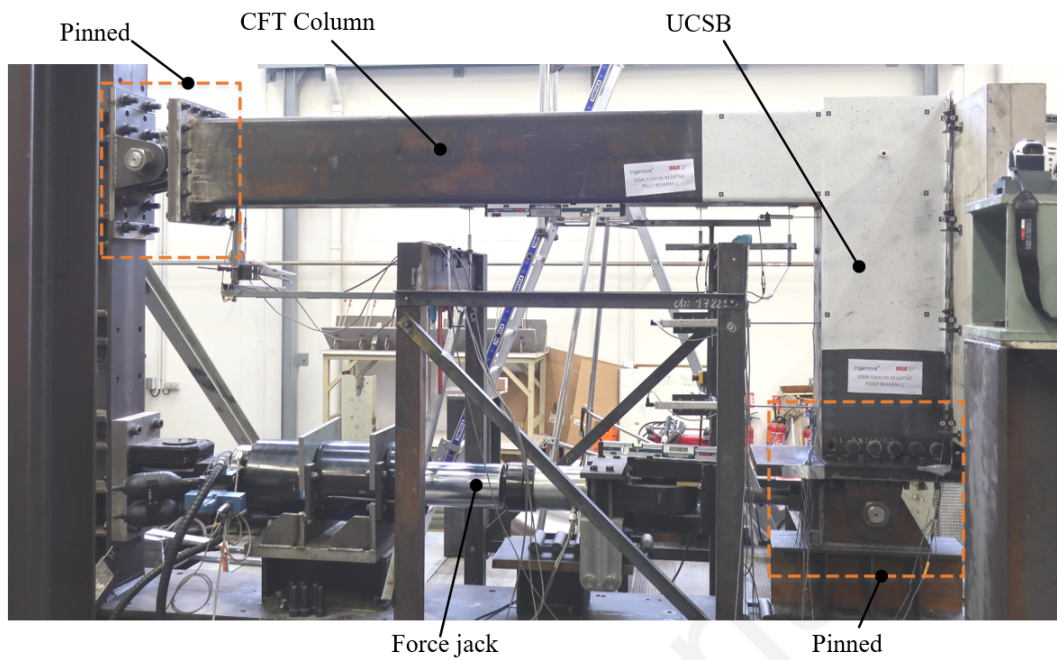


Figure 2: Actual photo of the test setup.

104 and the concrete beam at the load application point, a system of rigid steel element that is fixed to
 105 the pin and in contact with the concrete slab is added (see Fig. 4) so that the applied shear force
 is distributed to both the steel and the concrete.

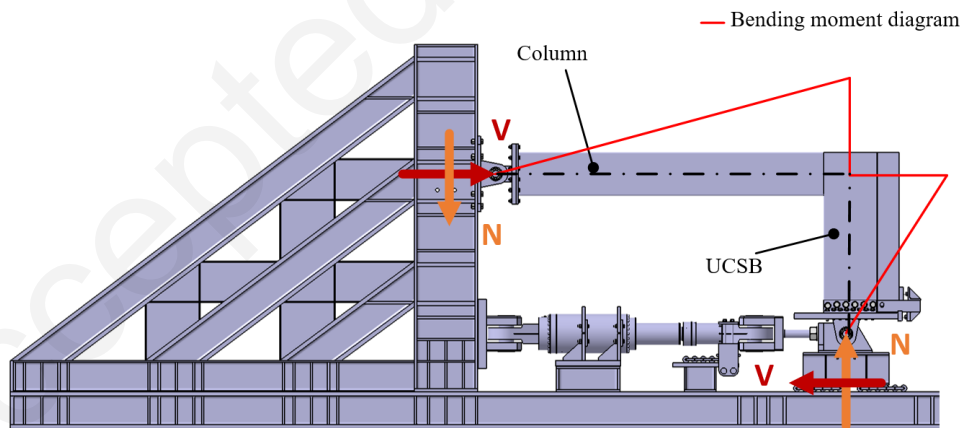


Figure 3: Reaction forces on the specimen.

106



Figure 4: System of rigid steel element for a good contact with the concrete.

107 *2.2. Specimen*

108 Two specimens (M_2^- and M_3^-) were fabricated for the experimental tests in this study. Each
 109 specimen (Fig. 5.a) consists of a composite beam with a cross-section shown in Fig. 5.b, two precast
 110 slabs, a composite column with a cross-section given in Fig. 5.c, and steel stiffeners placed in the
 joint (Fig. 6):

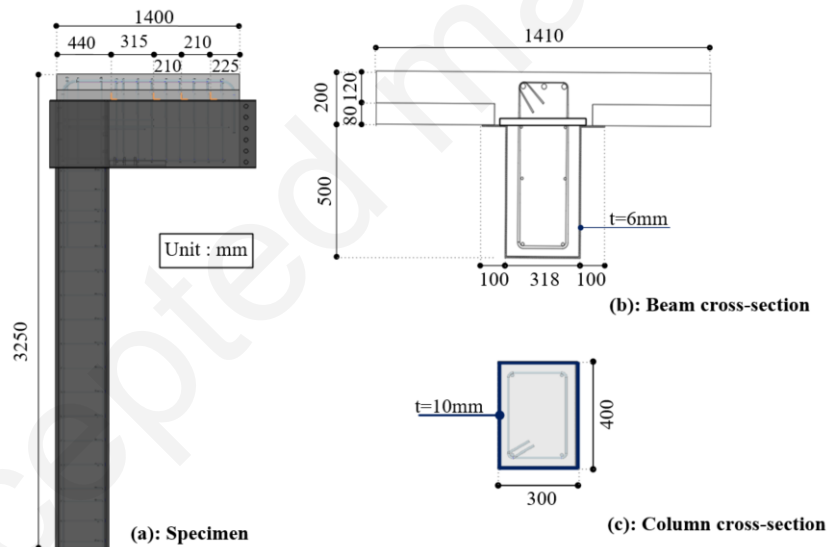


Figure 5: Dimensions of the test specimen.

- 111
- 112 - 4 L-shape connectors L50×50×5 mm (1) placed and welded on their periphery to the top
 113 flanges of the U-shaped steel girder with a contact length of 46mm;
- 114 - 3 steel angles L50×50×5 mm (2) welded to the external flange of the column. These steel
 115 angles are used for redistributing tensile forces from top steel HA20 rebars to the external

- 116 flange of the column;
- 117 - 6 steel pieces with a dimension of $70 \times 35 \times 15$ mm (3) for equilibrating the forces in compres-
- 118 sion in concrete and the steel;
- 119 - 2 stiffener plates $L78 \times 70 \times 8$ mm with a length of 400 mm (4) welded to bottom flanges and
- 120 webs of the U-shaped steel girder close to the hybrid joint in order to strengthen the bottom
- 121 flange and to avoid its buckling;
- 122 - 6 steel pieces with a dimension of $70 \times 35 \times 15$ mm (5), welded to the interior flange of the
- 123 column with V-hole for transferring compressive strut of the concrete to the junction node;
- 124 - A steel piece (6) welded to the inner surface of the column tube at the beam bottom level.

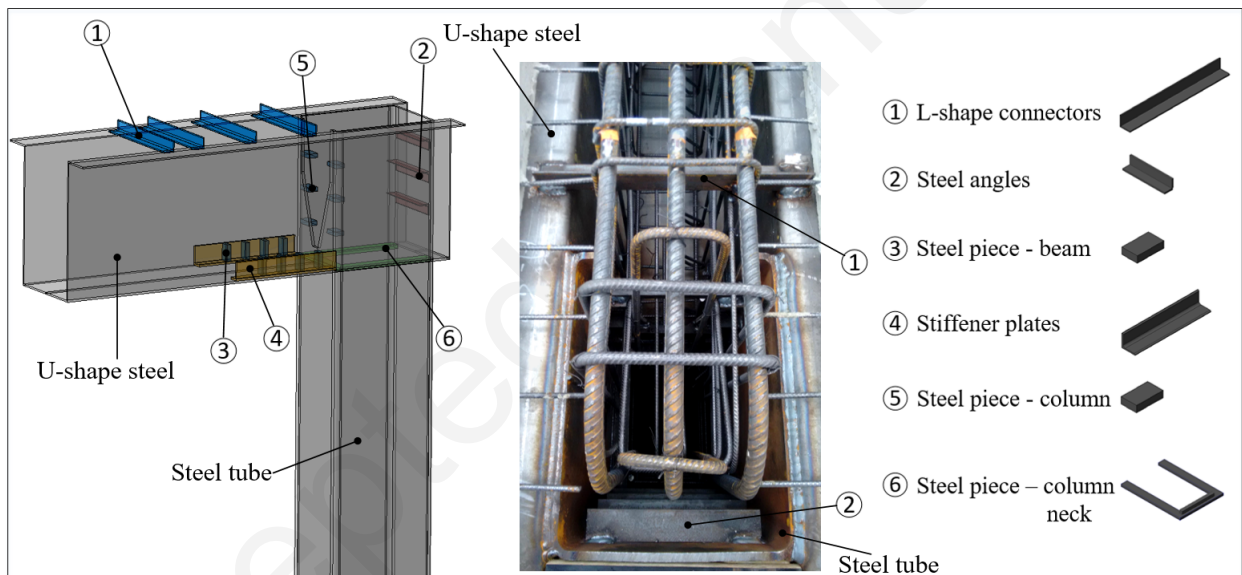


Figure 6: Components of the steel pieces in the specimen

125 All other details such as the dimensions and spacing of different components in the specimen are

126 provided in the Annex.

127 2.3. Material properties

128 In order to obtain the actual characteristics of the materials used on the day of experimental

129 tests, cylinder concrete tests on three specimens with a dimension of 11×22 cm were carried out for

130 the concrete material following the norm NF EN12390-3 [30], whereas one coupon test was made

131 for each steel material following the norm NF EN ISO 6892-1 [31]. The results are summarized
 132 in Table 1. f_{cm} is the mean value of concrete strength and σ_{cm} is its corresponding standard
 133 deviation, whereas E , f_y and f_u are the values of the Young modulus, the yield strength and the
 ultimate strength of steel, respectively.

Table 1: Material properties

Test	Concrete		Angles			Column			Beam			Rebars ($\phi 20$)		
	f_{cm}	σ_{cm}	E	f_y	f_u	E	f_y	f_u	E	f_y	f_u	E	f_y	f_u
	[MPa]	[MPa]	[GPa]	[MPa]	[MPa]	[GPa]	[MPa]	[MPa]	[GPa]	[MPa]	[MPa]	[GPa]	[MPa]	[MPa]
M_2^-	31.06	0.47	203	330	471	181	517	535	202	422	503	210	580	640
M_3^-	30.72	0.76												

134

135 2.4. Loading protocol and instrumentations

136 In the two tests (M_2^- and M_3^-), three phases of loading and unloading procedure were exerted
 137 before monotonically applying the load up to the collapse of the specimen:

- 138 - 5 cycles of loading and unloading between 10 kN and 85 kN ;
- 139 - 4 cycles of loading and unloading between 10 kN and 360 kN (value estimated for the service
 140 limit state design "SLS") ;
- 141 - 2 cycles of loading and unloading between 10 kN and 500 kN (value estimated for the ultimate
 142 limit state design "ULS") ;
- 143 - Loading up to collapse of the specimen.

144 It is important to note that the estimated load at the ULS was calculated based on an initial design
 145 model of the joint (see [18]), limiting the stresses at the plastification of the U-shaped profile and
 146 the rebars. The load at the SLS was grossly estimated to be equal to the value at the ULS divided
 147 by a coefficient of 1.4.

148 In order to obtain the moment-rotation curves and to observe the phenomena in the specimen,
 149 the following measurements (Fig. 7 and Fig. 8) were installed:

- 150 • Four vertical LVDT sensors under the column's interior flange with the capacity of 25 mm
 151 for C_{V1} and 100 mm for C_{V2} , C_{V3} and C_{V4} ;

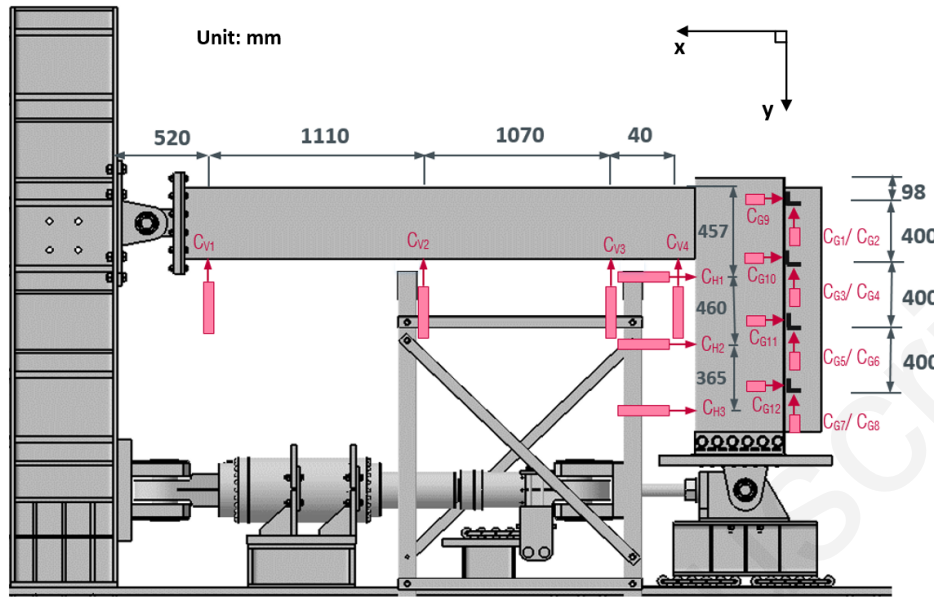


Figure 7: Vertical and horizontal LVDT sensors

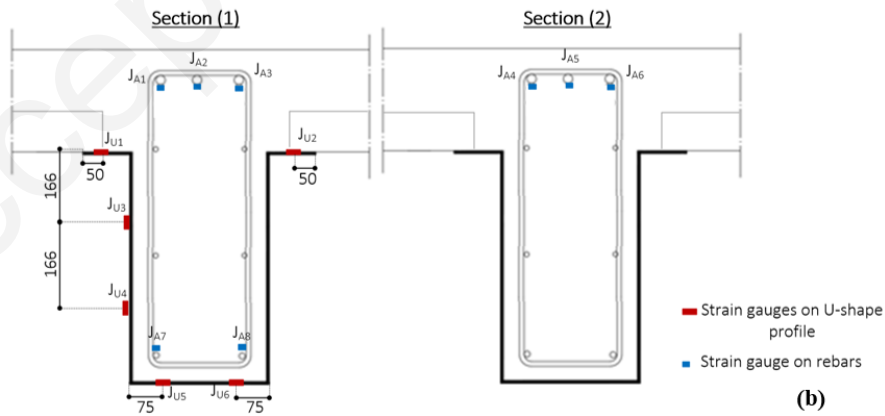
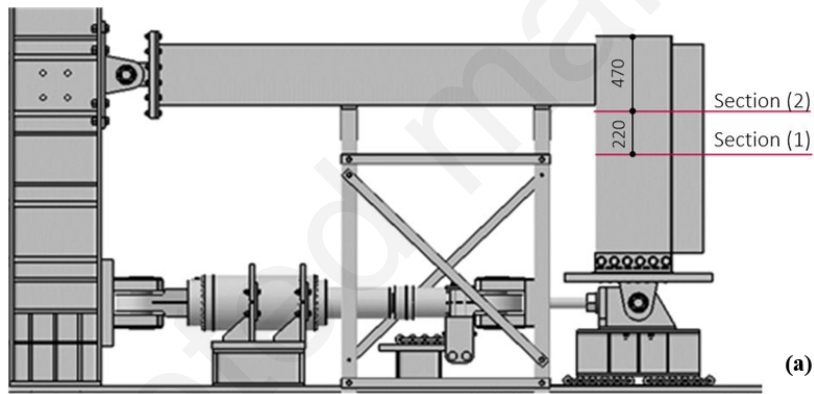


Figure 8: (a). Position of the sections. (b). Positions of strain gauges for U-shaped girder and HA20 rebars.

- 152 • Three horizontal LVDT sensors for the displacements of the beam with the capacity of 100
153 mm for C_{H1} and 300 mm for C_{H2} and C_{H3} ;
- 154 • Eight LVDT sensors C_{G1} to C_{G8} (4 at each side) for the relative displacements between the
155 concrete and steel (slips) with the capacity of 25 mm;
- 156 • Four LVDT sensors C_{G9} to C_{G12} for the separation between the concrete and steel (uplift)
157 with the capacity of ± 2.5 mm;
- 158 • Six strain gauges J_{U1} - J_{U6} for the deformations of the cross-section of the U-shaped girder
159 placed in section (1);
- 160 • Eight strain gauges J_{A1} - J_{A8} for the deformation of the steel rebars : 5 at section (1) (J_{A1} - J_{A3} ,
161 J_{A7} et J_{A8}) and 3 gauges at section (2) (J_{A4} - J_{A6}).

162 In addition to these analogue measurements, high resolution photo cameras were also installed
163 for an analysis using digital image correlation technology (DIC). The measuring areas of the DIC
are presented in Fig. 9. It should be noted that in the DIC technology, a series of photos is captured

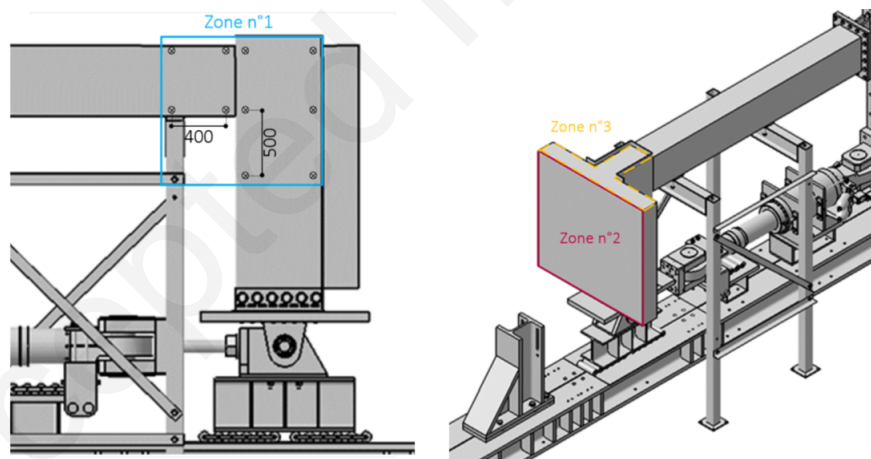


Figure 9: Zone for digital image correlation.

164 during the course of the test at each increment of loading by high resolution cameras. After the
165 tests, the photos are processed in order to obtain the strain field using GOM Correlate Professional
166 2016 [32].
167

168 *2.5. Results and discussions*

169 *2.5.1. Observations*

170 The phenomena observed during the test M_3^- are presented below with the help of the force-displacement curve, as illustrated in Fig. 10. Horizontal concrete cracks first developed on the

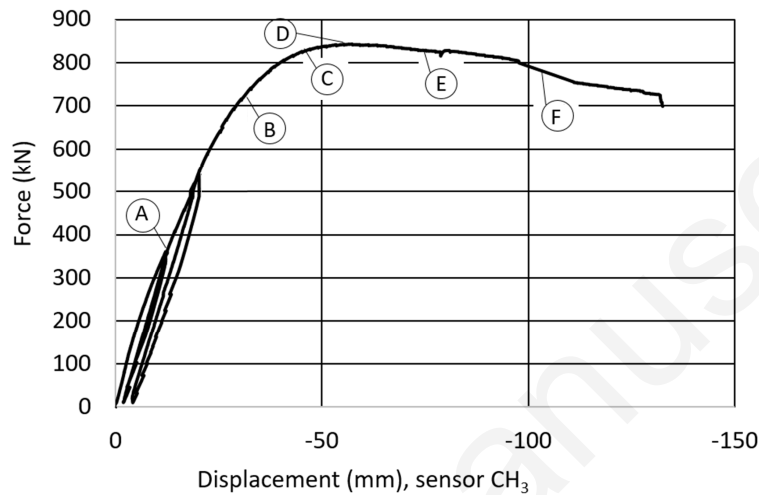


Figure 10: Force-displacement curve for test M_3^- .

171
 172 exterior surface of the concrete slab (zone 2, see Fig. 9) and at the back surface (zone 1, see Fig. 9
 173 and Fig. 11a) when the loading reached point A, which corresponds to the level of load at service
 174 limit state ($F=360$ kN). Later at point B ($F=715$ kN), a visible uplift between the concrete slab
 175 and the U-shaped steel girder at the top edge was noticed (Fig. 11b). After that, at point C ($F=817$
 176 kN), the initiation of buckling of the compressive flange of the column close to the hybrid joint was
 177 observed. The maximum load was attained at Point D ($F=842$ kN); at this point, the buckling
 178 was also visible in the webs of the column (Fig. 11c). Cracks in the welding between the flange of
 179 the beam and that of the column were then observed at point E ($F=836$ kN) (Fig. 11d). At point
 180 F, it can be deduced from the digital image correlation analysis that the steel has yielded at the
 181 column's neck and at the top part of the steel beam (see Fig. 11e). Fig. 12 shows the specimen
 182 after the test. Similar observations were also obtained during the test M_2^- .

183 *2.5.2. Analysis of measurements*

184 With the help from the analogue and digital measurements, the moment-rotation curve for each
 185 test are determined and presented in Fig. 13. The relative rotation of the joint θ obtained in the

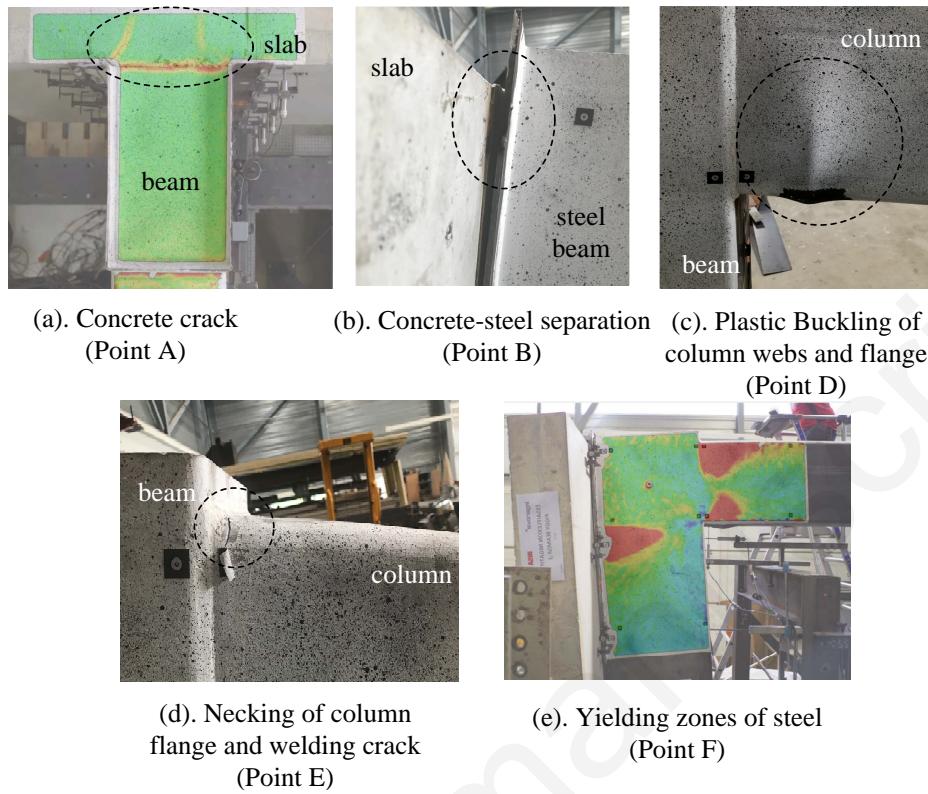


Figure 11: Experimental observations.



Figure 12: Specimen after the test.

186 figure is computed by

$$\theta = \alpha_1 - \alpha_2 \quad (1)$$

187 with

$$\alpha_1 = \arctan\left(\frac{\Delta V}{\Delta x}\right) \quad ; \quad \alpha_2 = \arctan\left(\frac{\Delta H}{\Delta y}\right) \quad (2)$$

188 where $\frac{\Delta V}{\Delta x}$ is the slope of the column at the joint side along column axis (x) and determined using
 189 sensors C_{V3} and C_{V4} , whereas $\frac{\Delta H}{\Delta y}$ is the slope of the beam along the beam axis (y) and determined
 190 using sensors C_{H1} , C_{H2} and C_{H3} . In addition, the bending moment is deduced by multiplying the
 191 force with the distance from column axis to the load application point.

192 The maximum rotation of the joints obtained in the two tests are larger than 0.04 rad; the
 193 joint is thus rather ductile. Based on EN1993-1-8 [20], within the configuration of the AVRIL
 194 building, it is possible to determine the classification of the joint with respect to its stiffness and
 its resistance. The initial stiffness $S_{j,ini}$ of the joint and the resisting moment $M_{j,R}$ can be defined

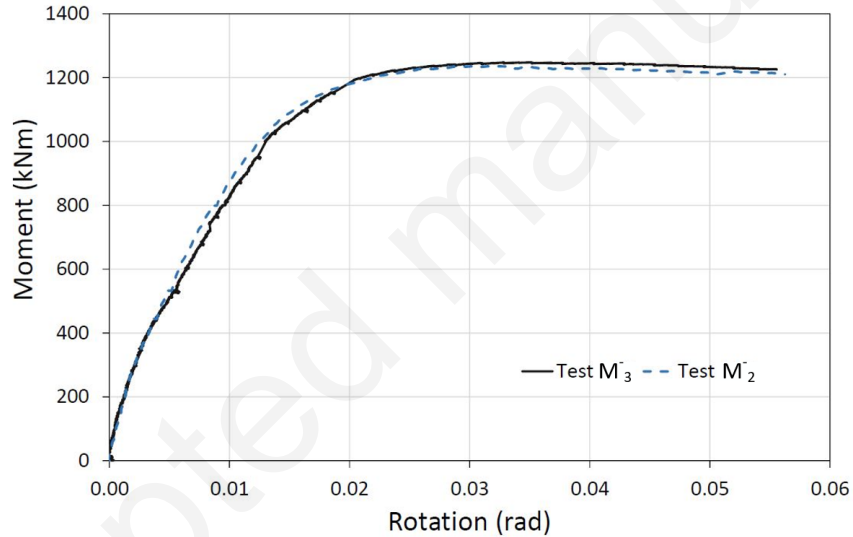


Figure 13: Moment-rotation curves.

195 by EN 1993-1-8 [20], as described graphically in Fig. 14. Their values obtained from the two tests
 196 are computed and provided in Table 2. Furthermore, the limits for considering the joint as rigid
 197 and as pinned are defined, respectively, as

$$S_{rigid} = \frac{25E_b I_b}{L_b} = \frac{25 \times 210000 \times 1.76 \times 10^9}{13.45 \times 1000} = 272063 \text{ kNm/rad} \quad (3)$$

$$S_{pinned} = \frac{0.5E_b I_b}{L_b} = \frac{0.5 \times 210000 \times 1.76 \times 10^9}{13.45 \times 1000} = 5441 \text{ kNm/rad} \quad (4)$$

200 By comparing the values obtained in Table 2 and those from Eqs. (3) and (4), the joint must be
 201 considered as semi-rigid.

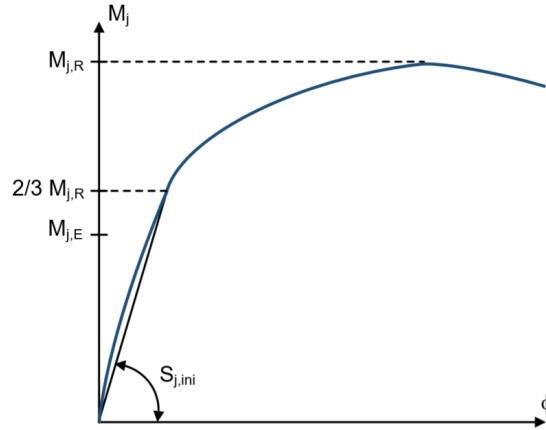


Figure 14: Initial stiffness ($M_{j,E} < M_{j,R}$) [20].

Table 2: Initial stiffness of the hybrid joint

Tests	$M_{j,R}$ [kNm]	$S_{j,ini}$ [kNm/rad]
M_2^-	1235	90113
M_3^-	1245	86395

202 The bending capacity of the beam cross-section with the actual characteristics of the materials
 203 is 1158 kNm. The maximum value of the bending moment of the joint obtained from the two tests
 204 is approximately 1235 kNm, calculated using the lever arm equal to the distance from the load
 205 application point to the column axis. It is therefore possible to conclude that the joint is fully
 206 resistant.

207 Figs. 15a and 15b illustrate the evolution of the slips along the beam axis for tests M_2^- and
 208 M_3^- , respectively. 0 mm corresponds to the position along the beam axis at the exterior flange
 209 of the column. The maximum attained load P_u for tests M_2^- and M_3^- are 833 kN and 842 kN,
 210 respectively. It can be seen from both figures that the slips at the positions closer to the zone of
 211 the joint are larger while those nearer to the beam edge (near the jack) are approximately zero.
 212 The distribution of the slips is consistent with the position of the connectors placed along the beam
 213 axis and with the level of applied bending moment.

214 Figs. 16a and 16b show the evolution of the uplifts along the beam axis for tests M_2^- and M_3^- ,
 215 respectively. Large uplifts are obtained in the zone where the column penetrates into the beam

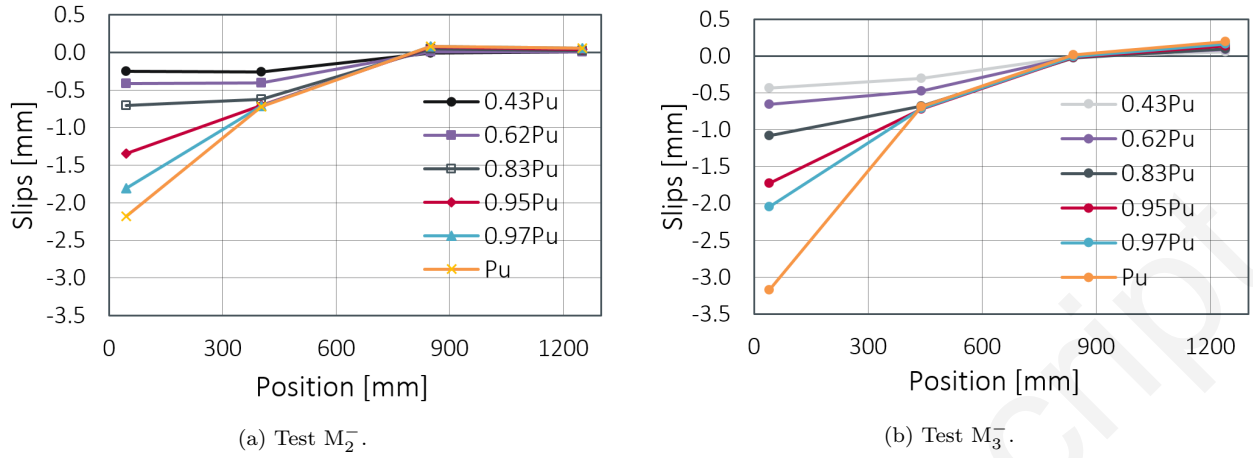


Figure 15: Evolution of slips along the beam axis.

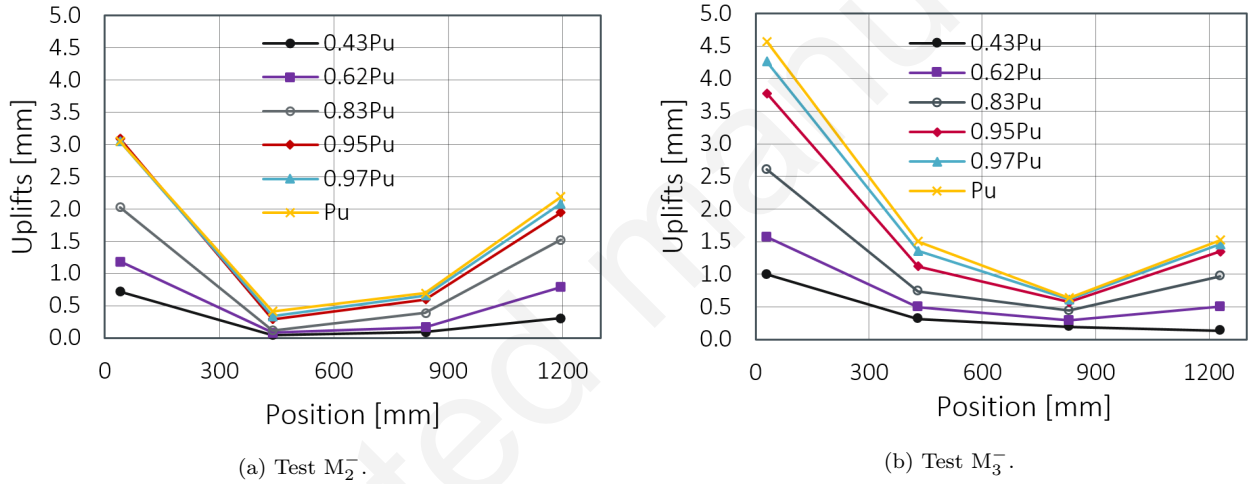
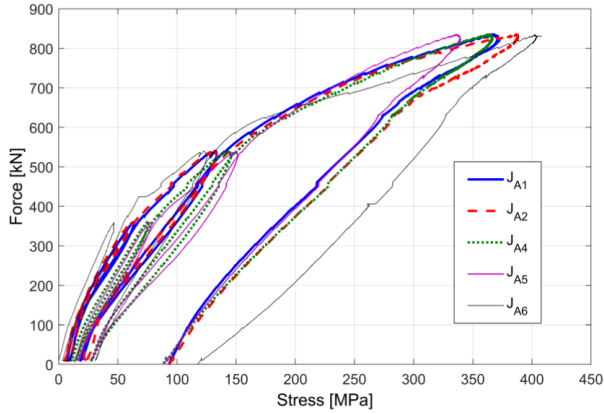


Figure 16: Evolution of uplifts along the beam axis ($P_u = 842$ kN).

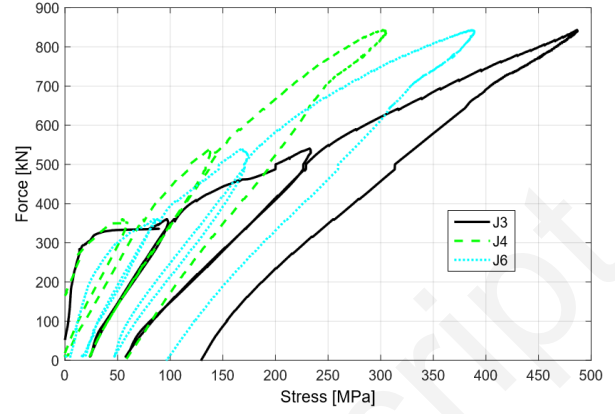
216 (between 0 and 400 mm). It is worth mentioning that there were not L-shape connectors in this
 217 zone.

218 Figs. 17a and 17b describe the evolution of the stresses on the rebars HA20 deduced from the
 219 strain gauge measurements in tests M_2^- and M_3^- , respectively. Only strains gauges (J_{A1} , J_{A2} , J_{A4} ,
 220 J_{A5} and J_{A6}) for M_2^- and (J_{A3} , J_{A4} and J_{A6}) for M_3^- are presented in these figures because the
 221 results obtained from the other strain gauges are erroneous. Since the yield limit is 580 MPa, the
 222 steel rebars at these locations have not yielded yet.

223 Figs. 18a and 18b describe the evolution of the stresses in the U-shaped steel girder obtained
 224 from the strain gauges for tests M_2^- and M_3^- , respectively. At collapse, the top flanges of the

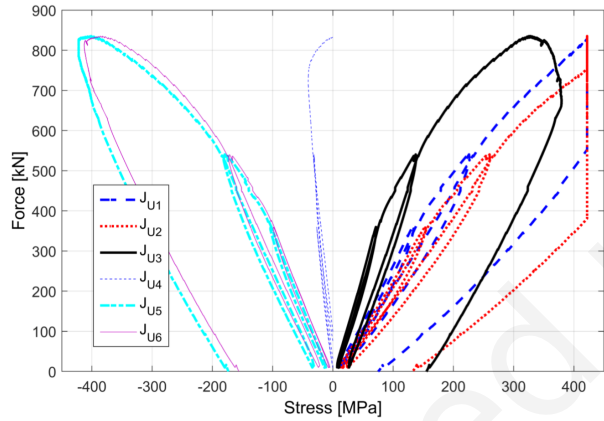


(a) Test M_2^- .

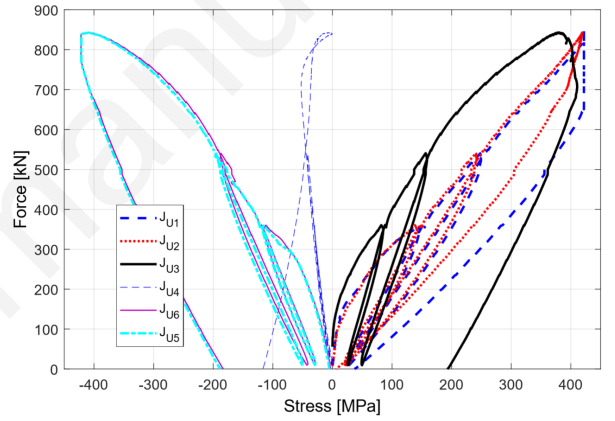


(b) Test M_3^- .

Figure 17: Evolution of stresses on rebars HA20.



(a) Test M_2^- .



(b) Test M_3^- .

Figure 18: Evolution of stresses on U-shaped steel girder.

225 U-shaped girder have yielded in test M_2^- (J_{U1} and J_{U2} , see Fig. 8a), as the yield limit of the steel
 226 girder is 422 MPa. On the other hand, in test M_3^- the top left flange (J_{U1}) has yielded while
 227 the other flange (J_{U2}) has almost yielded. The bottom flanges (J_{U5} and J_{U6}) have also yielded in
 228 compression for both M_2^- and M_3^- .

229 3. Finite element simulation

230 A full FE model of the test has been simulated in ABAQUS in order to acquire more information
 231 for a better understanding of the phenomena inside the specimen and to obtain the internal stress
 232 maps as well as cracking patterns for developing a design model of the joint. An explicit dynamic

233 analysis is chosen for this study. All the important components in the specimen are included, and
 234 the model is simulated in half with respect to a symmetric condition. The description of the FE
 235 model is provided in the following sections.

236 3.1. Element type and mesh

237 The components in the specimen were modelled using different types of elements. The concrete
 238 slab, the inside concrete beam (Fig. 19a) were meshed using the solid element type C3D10, a
 10-node quadratic tetrahedral element with 4 integration points. The in-filled concrete column

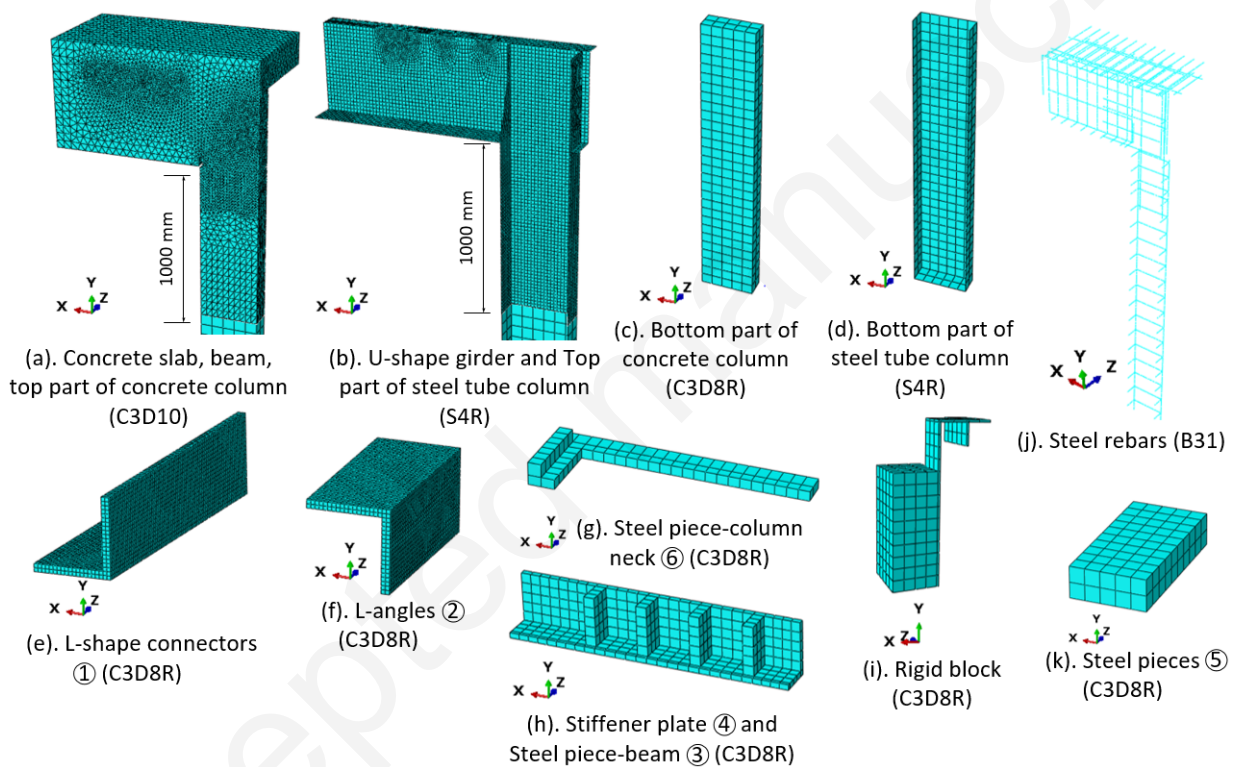


Figure 19: Meshing and element type.

239 was, on the other hand, modelled by two element types. The top part of the concrete column (Fig.
 240 19a) with a length of 1 m from the bottom surface of the beam was meshed using element type
 241 C3D10 whereas element type C3D8R (an 8-node brick element with reduced integration) was used
 242 for the bottom part (Fig. 19c). Furthermore, shell element type S4R, which is a 4-node doubly
 243 curved shell with reduced integration, was used for the U-shaped steel girder and the steel tube
 244 column (Figs. 19b and 19d). Two different element types or mesh sizes were used for the column
 245

246 because a fine mesh is required only in the zone close to the hybrid joint. While the steel rebars
 247 (Fig. 19j) were modelled by a 2-node beam element B31, the other steel components (Figs. 19e,
 248 19f, 19g, 19h, and 19k) were meshed by using the element type C3D8R (see Fig. 6 for the location
 249 inside the specimen). To apply the load on the pin as in the experiment, a rigid block (Fig. 19i)
 250 was created and meshed using the element type C3D8R.

251 3.2. Constraints and contact interactions

252 Explicit general contact interaction was used to define the contact behaviour of the concrete
 253 parts with U-shaped steel girder, steel tube column, and other steel pieces. The contact properties
 254 were defined by hard contact and friction penalty formulations for the normal and tangential
 255 behaviour, respectively. For the frictional contact, a friction coefficient of 0.5 was used. Besides,
 256 tie constraints were adopted for the contacts: between top and bottom parts of the concrete
 257 column, between top and bottom parts of the steel tube, between stiffener plate and steel pieces
 258 (Fig. 19h), between the L-shape connectors and the upper flanges of the U-shaped girder, between
 259 the L angles and the exterior flange of the column, between the rigid block and the cross section of
 the U-shaped girder, as well as between the rigid block and the concrete slab (Fig. 20a). However,

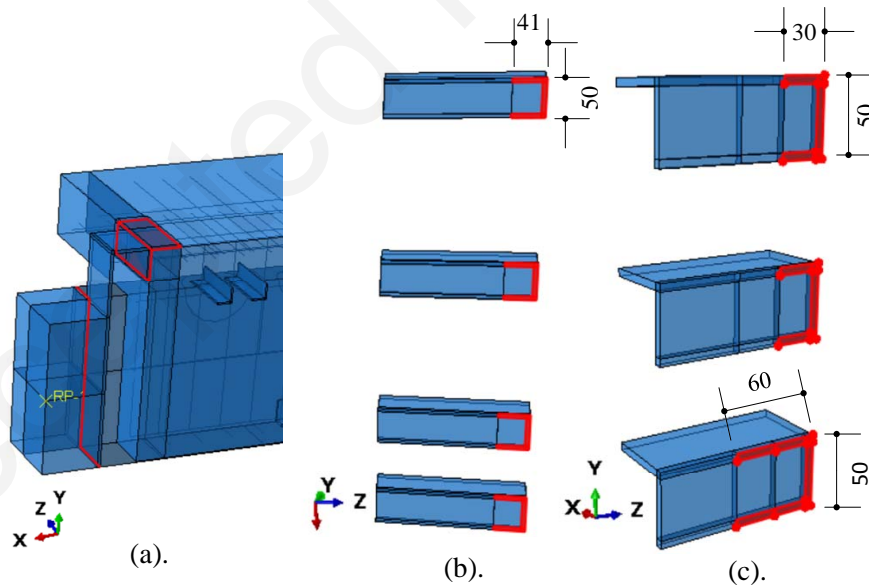


Figure 20: Tied surfaces.

260
 261 only certain surface areas between the L-shape connectors and the upper flanges of the U-shaped
 262 girder (Fig. 20b) and between the L angles and the exterior flange of the column (20c) were tied;

263 the rest of these contacts are frictionless. Apart from that, the embedded constraint was applied
264 to the rebars placed inside the concrete. At last, all nodes of the rigid block were constrained to a
265 reference point using a rigid body constraint.

266 3.3. Loading and boundary conditions

267 In order to obtain a quasi-static solution in the explicit dynamic analysis, a slow loading rate
268 with a smooth amplitude function was applied. Simulating only half of the specimen in a symmetric
269 configuration, a proper symmetric boundary condition was applied to selected surfaces and edges
270 constraining the displacement in Z-direction as illustrated in Fig. 21. Loading was applied to the
271 reference point that governs a rigid displacement of the rigid block through an imposed displacement
272 in Y-direction. The reference point was also fixed in all the remaining degrees of freedom except the
273 rotations. At the bottom edge of the column (a pin support), a middle edge along the Z-direction
274 was created and restrained in all the degrees of freedom except the rotation in the Z-direction.

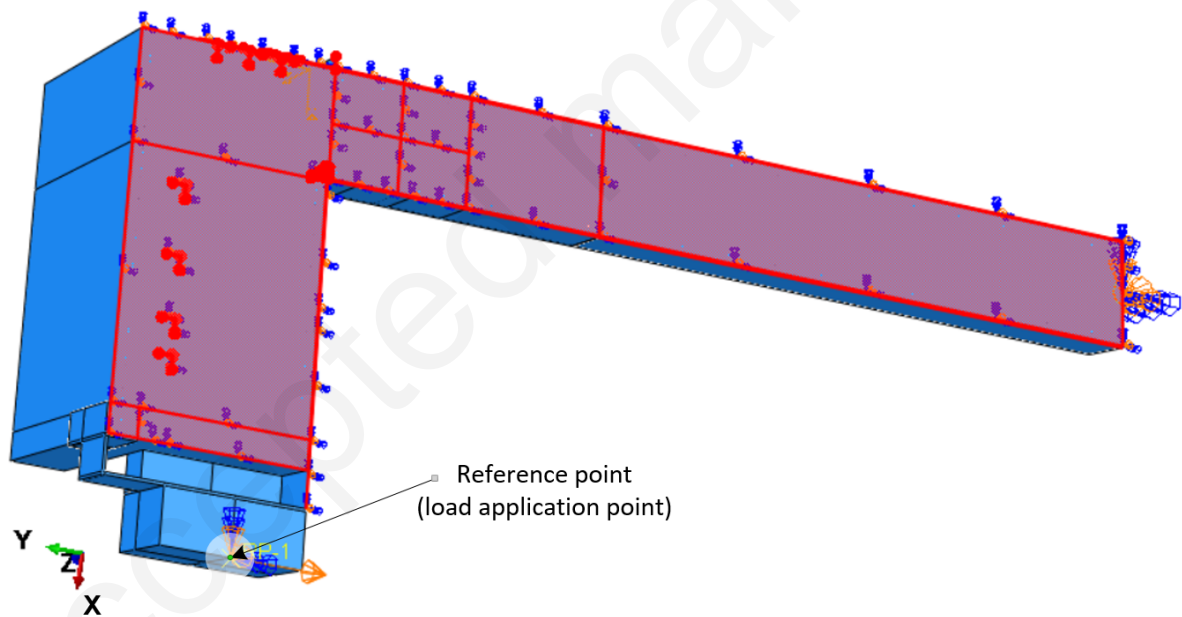


Figure 21: Loading and boundary conditions.

275 3.4. Material models

276 A concrete damaged plasticity model, which is available in ABAQUS, was used to model the
277 behaviour of the concrete. Default values for the parameters in the model were used except that
278 a large value of dilation angle of 52 degrees was adopted to capture the effect of highly confined

279 behaviour of the concrete, in some zones of the joints. A concrete constitutive model presented
 280 in [33, 17] was adopted. In the model, uni-axial compressive stress-strain and tensile stress-crack
 281 width curves (Fig. 22) were defined for the nonlinear behaviour of the concrete.

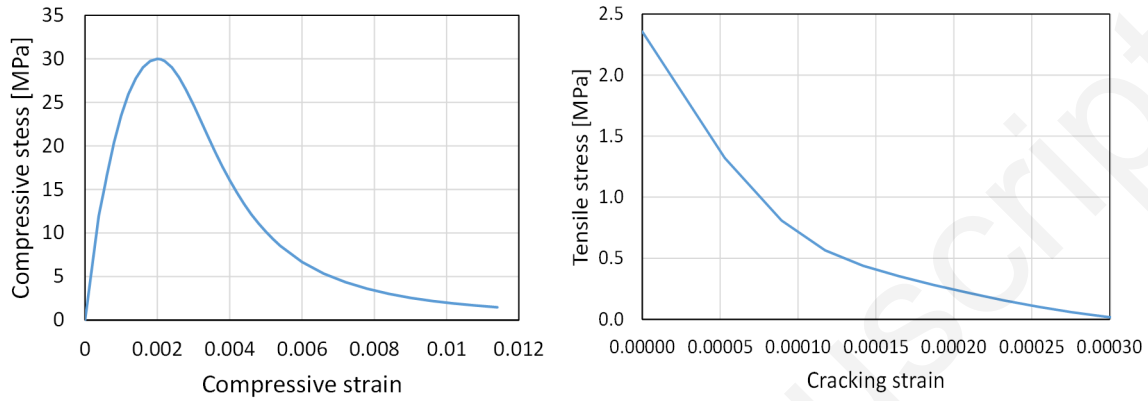


Figure 22: Constitutive concrete model.

282 Regarding the material model for steel, actual stress-strain curves obtained from coupon tests
 283 were used. In ABAQUS, true stress σ^{true} and true strain ϵ^{true} are input in the program. The
 284 Young's modulus of these materials are taken from Table 1.

285 3.5. Validation of the FE model

286 In order to validate the simulation, the results from the finite element model are compared
 287 with the ones obtained from the experiments. The failure modes and mechanical phenomena
 288 within the specimen are also investigated. The moment-rotation curves are compared in Fig. 23
 289 for specimen M_3^- . It can be seen that a good agreement between the two curves was achieved
 290 although a smaller initial stiffness in the FE model was observed probably due to the fact that
 291 chemical bonding between the steel and concrete was not included in the simulation.

292 Fig. 24 shows the comparison of uplifts (relative vertical displacements between U-shaped steel
 293 girder and concrete) along the beam axis between the results from FE model and experiment for
 294 specimen M_3^- obtained at the maximum load. It is shown that the distributions of the uplifts of
 295 the two results are in good agreement. However, a difference in uplift is found near the applied
 296 load location because a well constrained loading condition was adopted in the simulation whereas
 297 it is not the case in the experiment.

298 Fig. 25 shows the comparison of slips (relative horizontal displacements between U-shaped

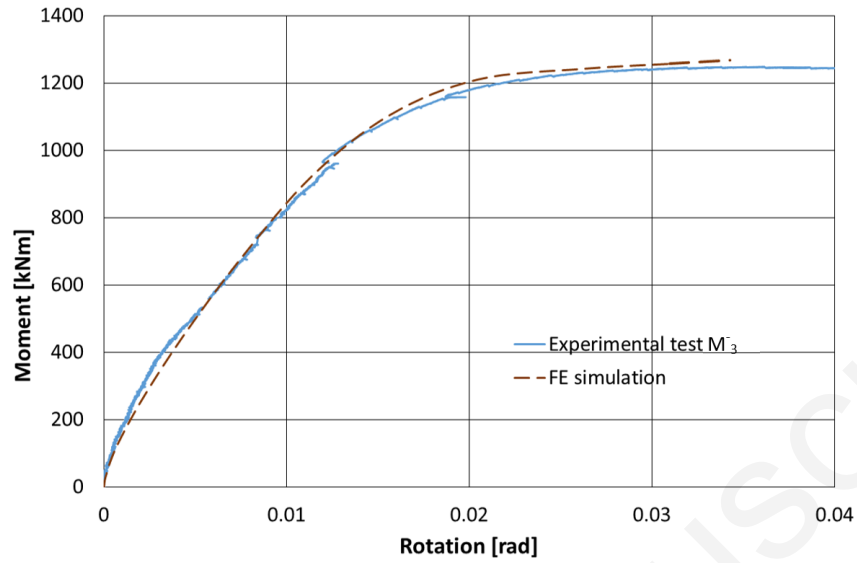


Figure 23: Comparison of moment-rotation curves obtained from FE simulation and from experimental test.

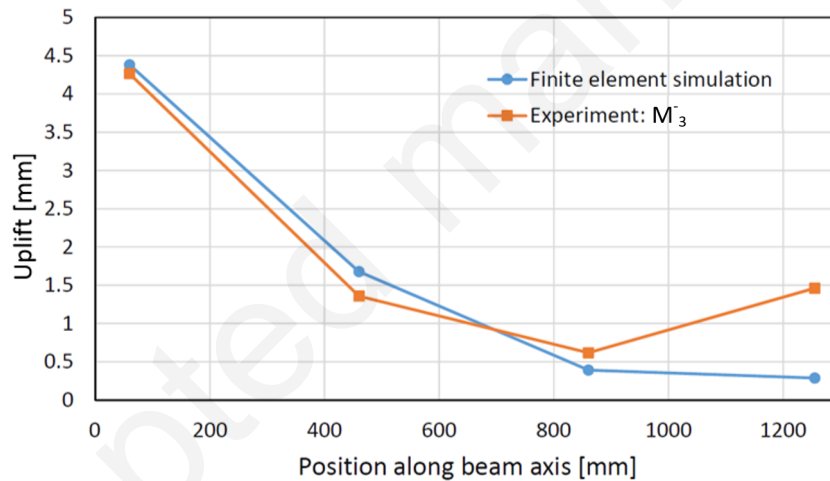


Figure 24: Comparison of uplifts obtained from FE simulation and from experimental test.

299 steel girder and concrete) along the beam axis between the results obtained from FE model and
 300 experiment for specimen M_3 at the maximum load. It can be observed that the distribution of the
 301 slips is similar in both results.

302 In addition, the experimental specimens were cut along two planes, as illustrated in Fig. 26,
 303 in order to see the cracking patterns within the joint. The cutting plane A-A is shown in Fig. 27
 304 with a side-by-side comparison between the cracking patterns in the specimen (Fig. 27a) and the
 305 equivalent plastic strain (PEEQ) in the concrete of the FE simulation (Fig. 27b); the scale limit of

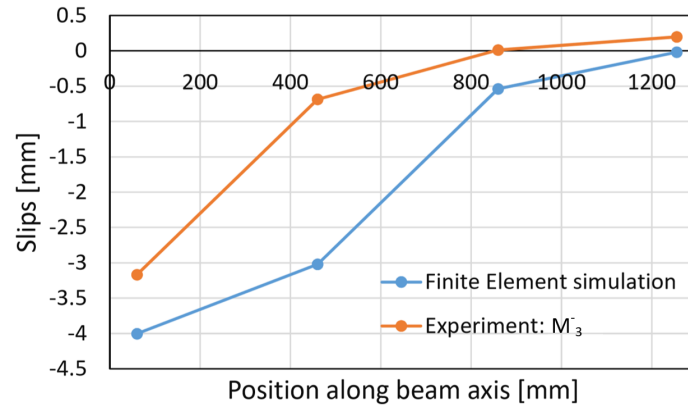


Figure 25: Comparison of slips obtained from FE simulation and from experimental test.

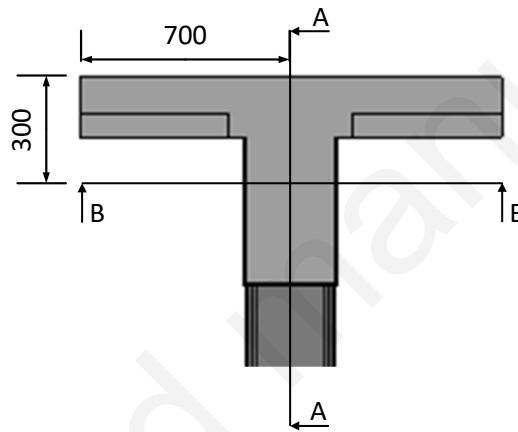


Figure 26: Positions of cutting planes of the specimen.

306 the PEEQ is 5×10^{-3} in this figure. Most of the cracking patterns in the specimen can be found
 307 in the plastic strain map of the FE simulation. The crushing of the concrete at the zone where
 308 the interior flange of the column is buckled (failure mode) is also observed in the FE simulation.
 309 Fig. 28 shows the zoom version of the cutting plane A-A at the zone of the three steel angles. In
 310 this figure, the limit of the PEEQ is scaled to 2×10^{-2} in order to better show the plastic strain
 311 pattern. A vertical crack is also visualized at the edge of the L-angles. The cutting plane B-B,
 312 illustrated in Fig. 29, also shows the same comparison. The cracking on the left side aligned with
 313 the three vertical HA20s is found in both the experiment and the simulation. The strain field on
 314 the steel part obtained from the DIC in the test is also compared with the strain map obtained in
 315 the FE simulation, as can be seen in Fig. 30. The yielding zones appear to well resemble in the
 316 two cases.

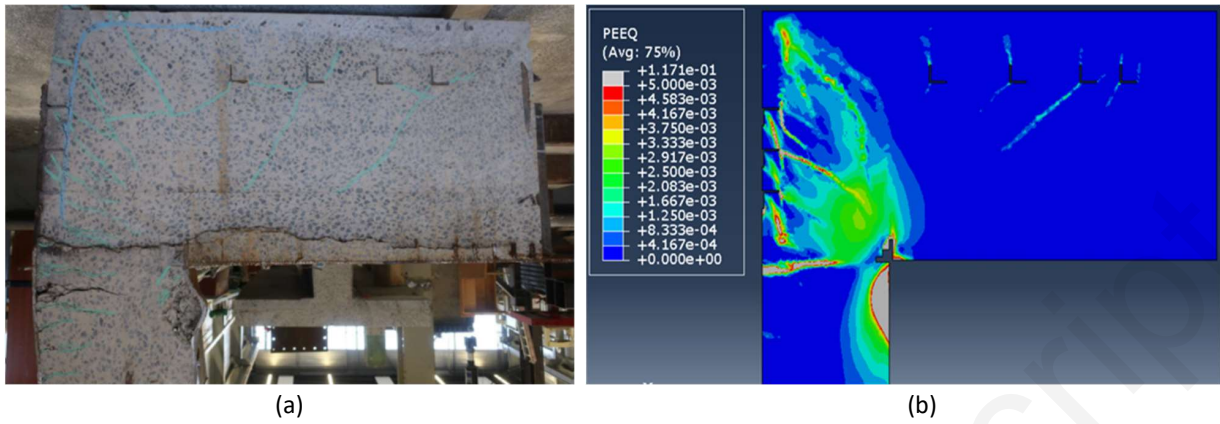


Figure 27: Section A-A: (a). Cracking patterns in specimen (b). Plastic strain PEEQ of FE model.

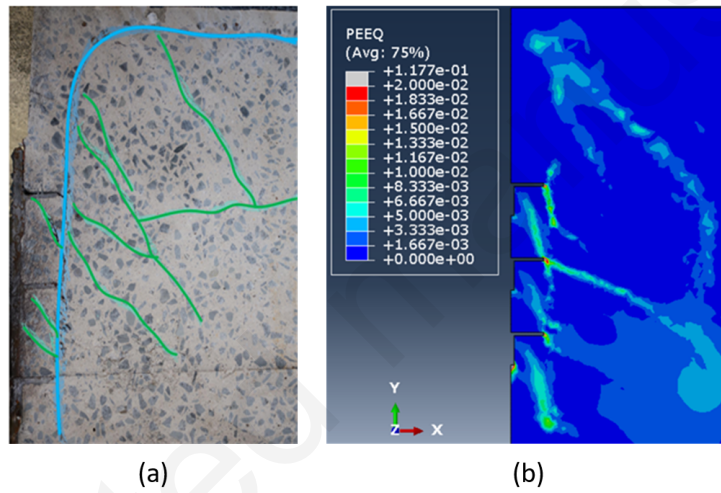


Figure 28: Zoom of section A-A: (a). Cracking patterns in specimen (b). Plastic strain PEEQ of FE model.

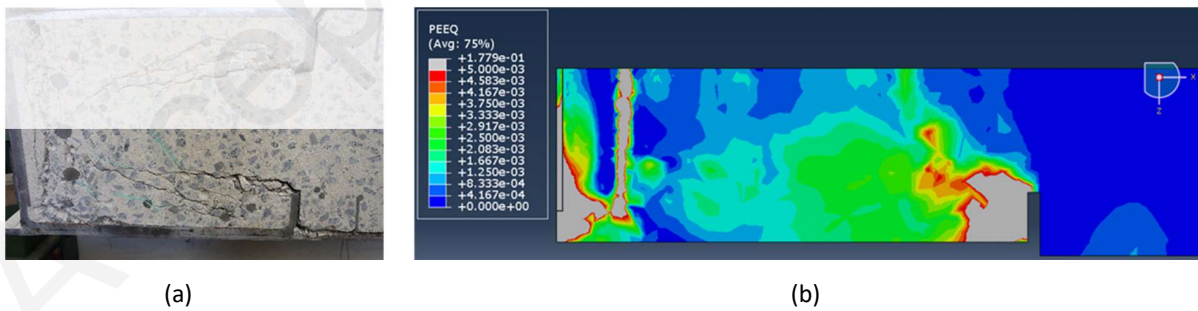


Figure 29: Section B-B: (a). Cracking patterns in specimen (b). Plastic strain PEEQ of FE model.

317 All in all, the results obtained from the FE model are in good agreement with the experimental
 318 observations. The FE model is able to reproduce the global behaviours such as moment-rotation

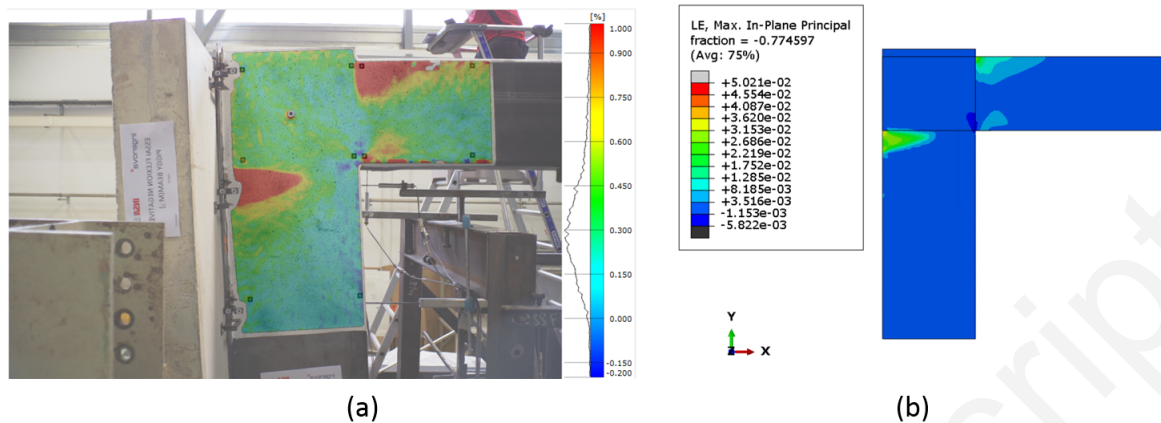


Figure 30: Steel part of the joint: (a). Strain field from Digital Image Correlation. (b). Strain map from FE simulation.

319 curve, the distribution of the uplifts and the slips, as well as the degradation of the materials
 320 (cracking and crushing of the concrete as well as yielding of steel) observed in the experimental
 321 tests. It can then be concluded that the FE model has been well validated against the experimental
 322 tests.

323 The numerical model allows to enhance the experimental observations concerning the propa-
 324 gation of the material yielding in the specimen. The following information on the yielding order of
 325 the materials are deduced from the numerical results. The vertical part of the rebars H20 was the
 326 first to yield. It was then followed by the plastification of the U steel profile at the cross-section
 327 that is close to the joint (see Fig. 30). The cross-section of the column at the neck is the last to
 328 yield, leading to the decrease of the load.

329 It can also be concluded that the maximum load is limited by the yielding of the cross-section
 330 of the steel column at the intersection with the beam, whereas some reserves are still available in
 331 the U-shaped steel profile as well as in the shear steel panel of the joint. It is thus important that
 332 the design model reproduces these observations.

333 4. Proposed design model for the joint

334 Whereas the USCBC has a composite cross-section, in which steel and concrete contribute sig-
 335 nificantly to the flexural resistance of the beam, the resistance in the composite column is mainly
 336 provided by the steel section. As a consequence, the design model of the joint has to take into
 337 account the transfer of forces between the two materials. It is thus a combination of a model of

338 the reinforced concrete joint and a model of the steel joint with a system of force transfer mecha-
 339 nisms between both models. The dimensions of the joint model and the distributions of the forces
 340 between the parts in the joint are determined in the following sections.

341 4.1. Dimensions of the model

342 Usually, models of beam-to-column joints are limited to the D-region where the beam theory
 343 is not applicable. As in the test the load is applied close to the end of the D-zone of the beam, the
 344 model is extended to the whole beam. The positions of the end sections of the model are depicted
 in Fig. 31.

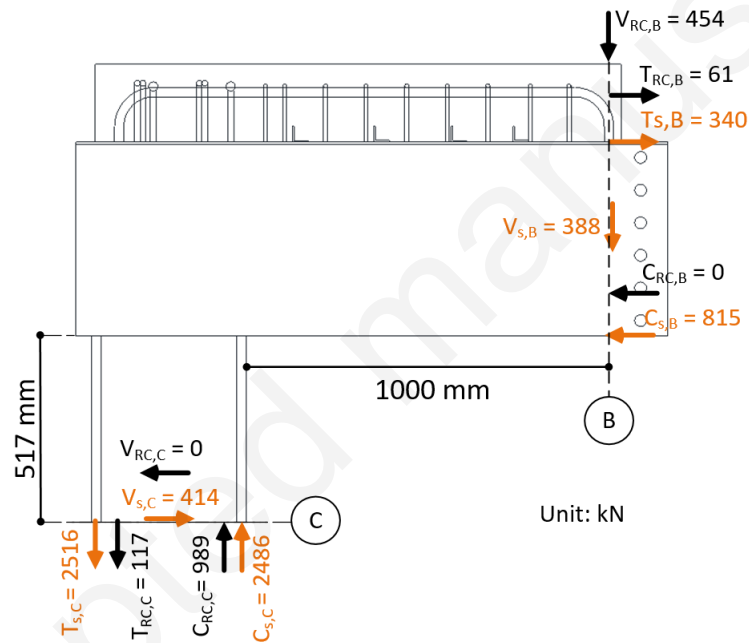


Figure 31: Positions of cross-sections of the joint for the model and its forces.

345
 346 The design model is developed for the maximum force obtained from the FE simulation $P_u =$
 347 842 kN . The normal force N_{Ed} , the shear force V_{Ed} and the bending moment M_{Ed} applied to the
 348 beam section B and to the column section C are reported in Table 3. As the joint is a combination
 349 of a concrete part and a steel part, it is necessary to determine the distribution of these global
 350 forces between the concrete and the steel parts of the joint. Since the experimental measurements
 351 did not provide information on the distribution of the forces between the different materials of the
 352 cross-sections, it is deduced from the numerical simulation and provided in Fig. 31. In the figure,

353 T and C denote the tensile and the compressive forces, respectively. The subscripts RC, S, C, and
 354 B stand for reinforced concrete, steel, column and beam.

Table 3: Total forces on the cross-sections

Section C			Section B		
$N_{Ed,C}$ [kN]	$V_{Ed,C}$ [kN]	$M_{Ed,C}$ [kNm]	$N_{Ed,B}$ [kN]	$V_{Ed,B}$ [kN]	$M_{Ed,B}$ [kNm]
-842	-414	-950	-414	-842	-328

354

355 4.2. Model for the reinforced concrete part of the joint

356 Strut-and-tie models are usually considered for the design of concrete beam-to-column joints.
 357 These models are rather simple, and their design provision can be found in design standards, for
 358 example Eurocode 2 [19]. The forces applied in the beam section are balanced with the forces in
 the column by means of multiple diagonal struts, as shown in Fig. 32. For the particular case of

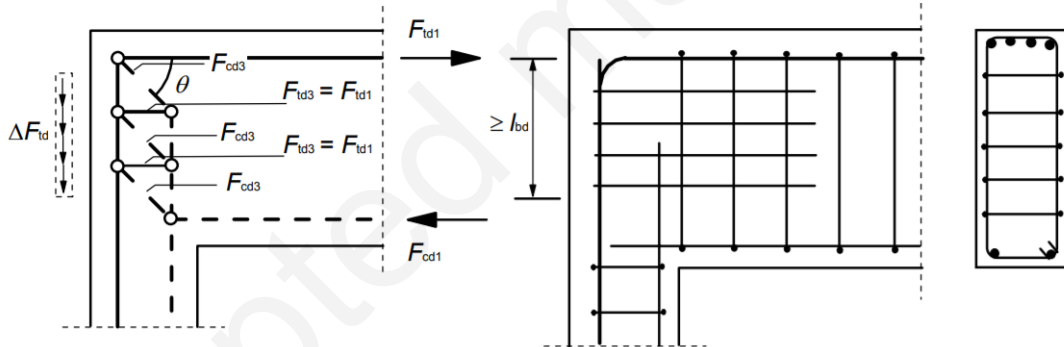


Figure 32: Frame corner with closing moment for very different depth of beam and column [19].

359

360 the joint handled in this article, the geometry of the concrete strut-and-tie model is defined based
 361 on the principal stress map obtained from the FE model as illustrated in Fig. 33. In this figure,
 362 the struts are represented by dashed lines and the ties by continuous lines. The black arrows are
 363 the forces applied on the cross-sections of the reinforced concrete, and the blue ones are the forces
 364 that are transferred from the steel joint. The nodes are numbered from 1 to 14; the struts and the
 365 ties are notated by C_{i-j} and T_{i-j} , connecting node i to node j .

366 The justification of the choice for the geometry is given as following:

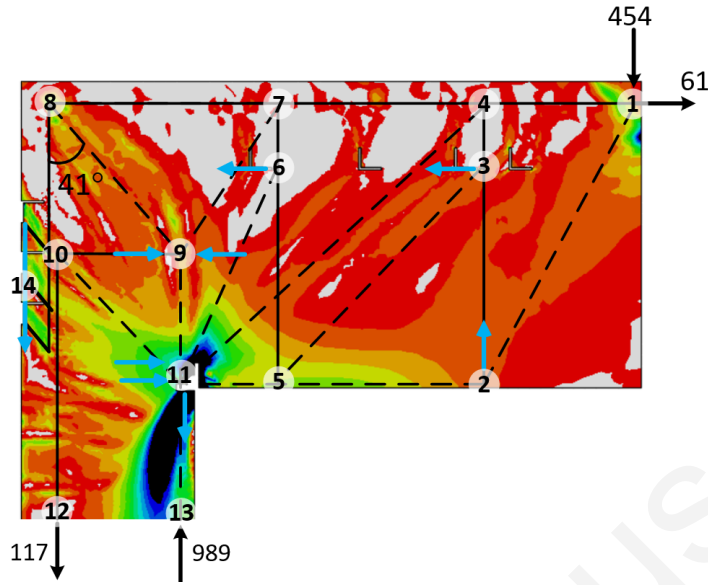


Figure 33: Geometry of the strut-and-tie model deduced from principal stress maps of FE Model.

- 367 • The diagonal strut C_{1-2} is fixed by the application point of the load (node 1) and follows
368 the orientation of the large compressive stress;
- 369 • The diagonal struts C_{3-5} , C_{4-11} , C_{7-9} and C_{8-9} are positioned at the location where the FE
370 model shows apparent large compressive stress patterns. The height of node 3 is fixed by the
371 position of steel-concrete L-shape connectors;
- 372 • The FE model brings to light the existence of two diagonal struts, C_{8-9} and C_{10-11} , within
373 the joint. Their geometry is consistent with the limit imposed by Eurocode 2 ($\tan \theta > 0.4$).

374 The dimensions of the model and the resulting forces in the struts and the ties are given in
375 Fig. 34 and Fig. 35, respectively. The following remarks should also be noted:

- 376 • The flexural tensile force generated by the external loads applied to the concrete cannot be
377 balanced by the top HA20 rebars. As a consequence, a part of the tensile force is transmitted
378 to the upper flanges of the U-shaped beam through shears connectors at nodes 3 and 6, as
379 highlighted by blue arrows in Figs. 33, 34 and 35. This explains the existence of the struts
380 C_{3-5} , C_{4-11} , C_{6-11} , and C_{7-9} .
- 381 • The tensile force in the vertical part of the HA20 rebars T_{8-10} is balanced by the HA12 rebars
382 T_{10-12} , by the exterior flange of the steel column through the three L-angles, as well as by

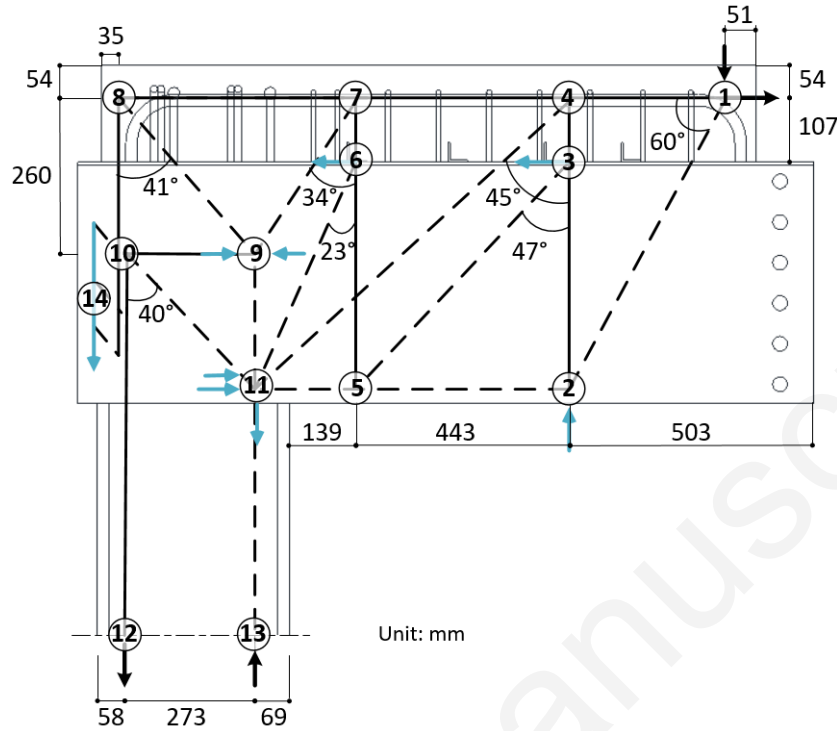


Figure 34: Dimensions of strut-and-tie model of reinforced concrete joint.

- 383 the strut C_{10-11} .
- 384 • The struts C_{7-9} and C_{8-9} generate compressive forces onto node 9. These diagonal compressive forces are balanced by a vertical compressive force in concrete C_{9-11} , the tensile forces in stirrups (T_{9-10}) and the horizontal forces transmitted from the steel joint (blue arrows at node 9). It must be pointed out that the rebars constituting the tie T_{9-10} have yielded. In the same way, the equilibrium of node 11 is justified by the forces transferred from the steel joint.
- 385
- 386
- 387
- 388
- 389
- 390 • The vertical tie T_{2-3} (A sum of 5 HA8 stirrups) is not able to resist to all the vertical applied force ($F=454$ kN). A part of it is immediately transmitted to the bottom flange of the U-shaped steel beam at node 2 by concrete pressure. It is further detailed in the next section.
- 391
- 392
- 393
- 394 In the design model, the tie T_{8-10} is the first to yield, which corresponds well to the observation made in the numerical simulation. The detailed verification of each node of the model is not presented here. It can be found in the PhD thesis by Lepourry [34].
- 395
- 396

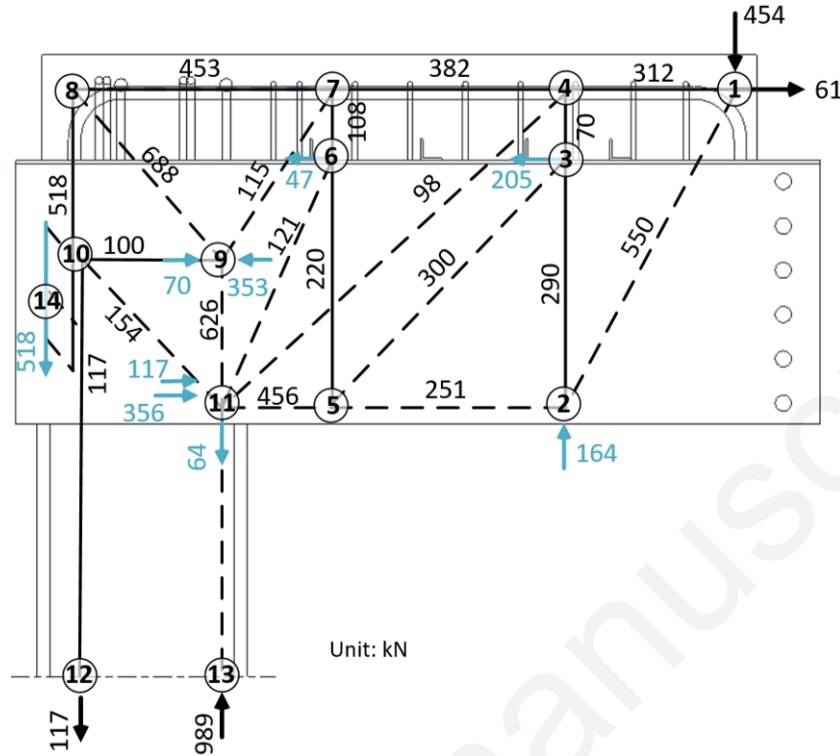


Figure 35: Forces in the strut-and-tie model.

4.3. Load transfer mechanism between steel and concrete in the joint

The load transfer between steel and concrete happens in different zones, which are illustrated in Fig. 36. A more detailed description of these zones are given as following (see Fig. 37):

- As already explained, in zone 1, the tensile force in the rebars HA20 is transmitted to the outer flange of the column through 3 L-angles ($F_{T,s1} = F_{T,RC1} = 518$ kN). The transferring is made through inclined short struts that develop horizontal tensile forces in these zones. These tensile forces are not well balanced and cause horizontal cracks in concrete, which were observed in the specimen after the experimental tests (Fig. 28a).
- In zone 2, the L-angles welded to the upper flanges of the U-shaped profile play their role of shear connectors to transfer horizontal forces from concrete to upper flanges of the U-shaped steel profile ($F_{T,RC2} = F_{T,s2} = 252$ kN).
- In zone 3, the horizontal components of compressive struts C_{4-11} , C_{6-11} , C_{7-9} and C_{8-9} are applied to the inner flange of the steel column by contact interfaces between the inner flange

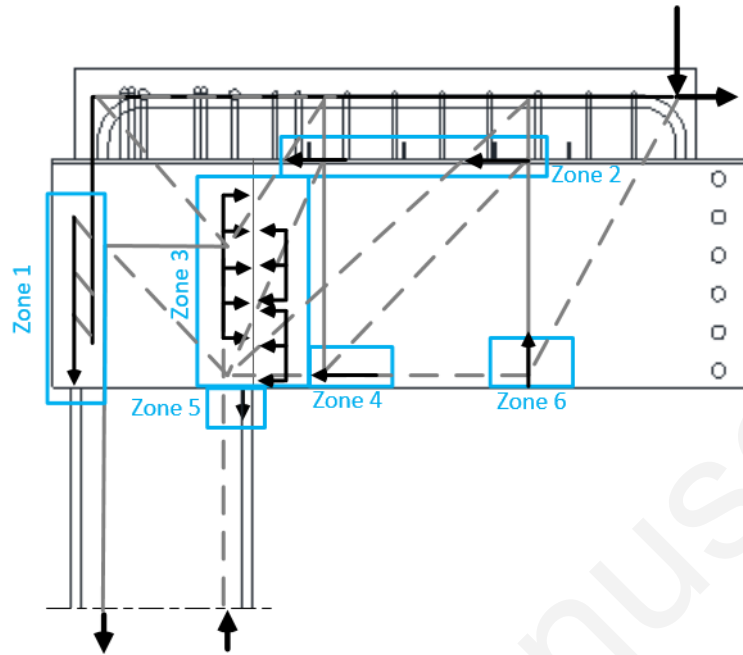


Figure 36: Zones of load-transferring between the steel and the concrete.

410 of the column and those of the concrete.

- 411 • In zone 4, a compressive force is transferred from the concrete to the lower flange of the U
- 412 element through 8 steel pieces welded to 2 steel reinforced angles that are themselves welded
- 413 to the bottom flange of the steel beam.
- 414 • Since in zone 5 most of the compressive force are taken by the interior flange of the steel
- 415 column, only a small portion of this vertical compressive force ($F_{C,s5} = F_{C,RC5} = 64 \text{ kN}$) is
- 416 transmitted to concrete from steel through the steel piece that is welded to the interior flange
- 417 of the steel column.
- 418 • For zone 6, as mentioned earlier, the applied force of 454 kN is balanced in part by the tie
- 419 T_{2-3} , whereas the rest ($F_{C,s6} = F_{C,RC6} = 164 \text{ kN}$) is balanced by the U-shaped profile by
- 420 concrete pressure.

421 4.4. Model for the steel part of the joint

422 The transferring of forces from the concrete to the steel have to be taken into account in the

423 model. Fig. 38a illustrates the forces applied to the cross-section of the steel beam and the steel

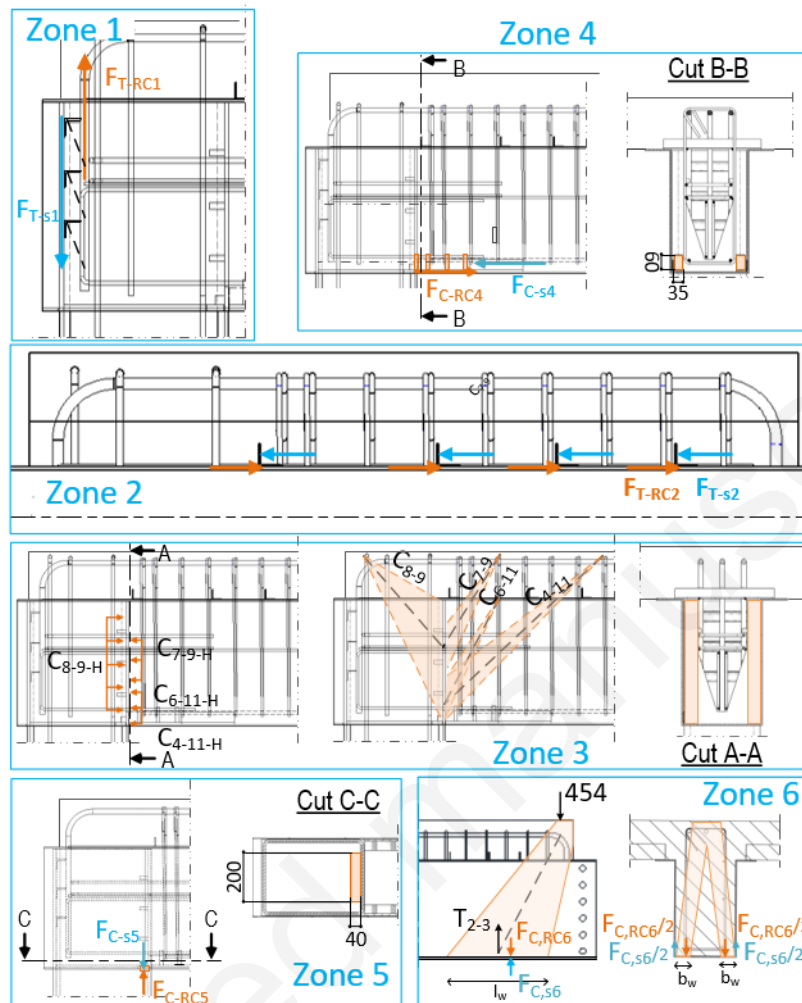


Figure 37: Detail of the load-transferring zones between the steel and the concrete.

424 column, as well as the ones (orange arrows) added to the steel joint from the concrete part. The
 425 steel joint model is rather usual : compressive and tensile forces generated by the bending moment
 426 in the U-shaped profile are balanced by the ones in the steel column through two web panels.
 427 Resulting forces applied to the two shear panels are given in Fig. 38b.

428 The total thickness of each shear panel is 16 mm, because the panel is composed of a web of
 429 the column with a thickness of 10 mm and a web of the U-shaped steel profile with a thickness of
 430 6 mm. As the horizontal force (283 kN, see Fig. 38b) is applied to the shear panel, the shear panel
 431 is subdivided into two sub-panels, as it was also done in [35, 36, 37]. Moreover, the flanges of the
 432 beam and of the column are not able to withstand the tensile and compressive forces generated by
 433 the bending moment into the joint. As a consequence, parts of the webs next to the flanges are

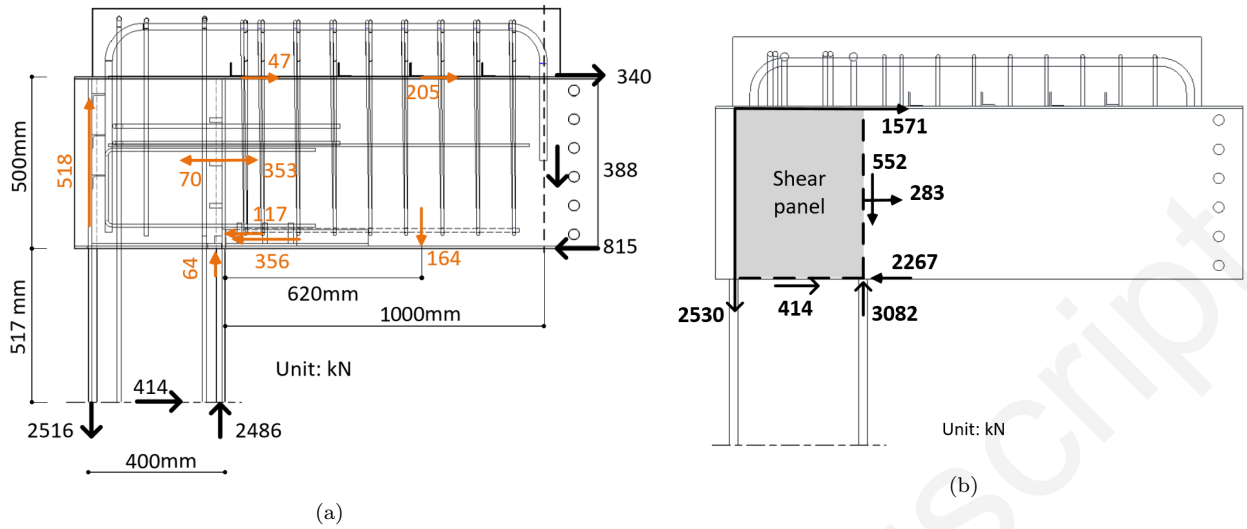


Figure 38: (a). Forces applied on the steel part of the joint. (b). Forces applied to shear panels

434 considered to take axial stresses. The detailed description of the forces acting in one shear panel is given in Fig. 39 by zones. The geometrical description of these zones is given in Fig. 40.

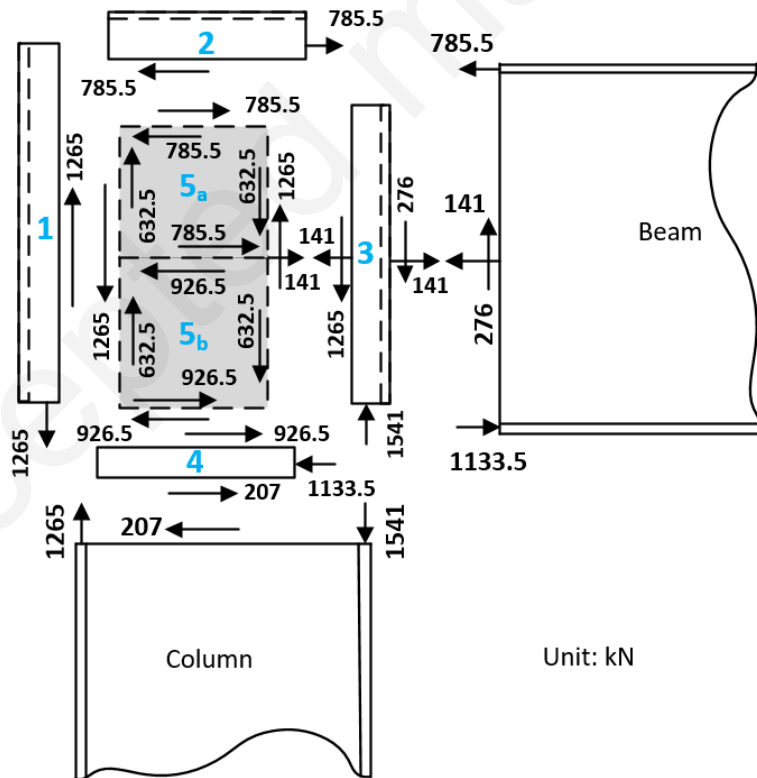


Figure 39: Zones of shear panel.

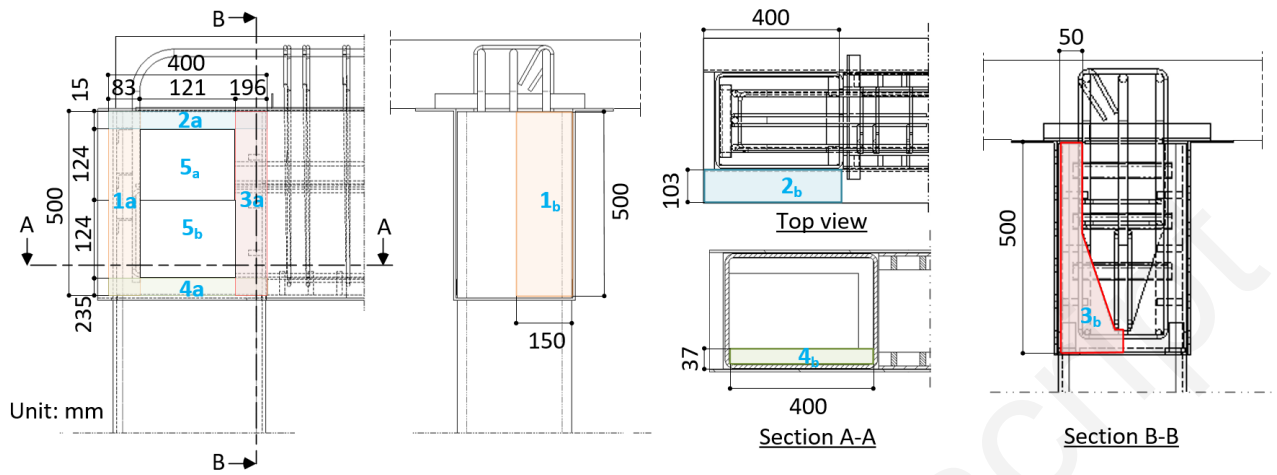


Figure 40: Dimensions of sub-zones.

436 **5. Propositions for the optimization of the joint.**

437 The verification of the joint by the design model brought to light the fact that some steel pieces
 438 placed in the joint that take part in the load-transferring system do not have an optimal behaviour,
 or might be unnecessary. Consequently, this section presents a proposed numerical study on some

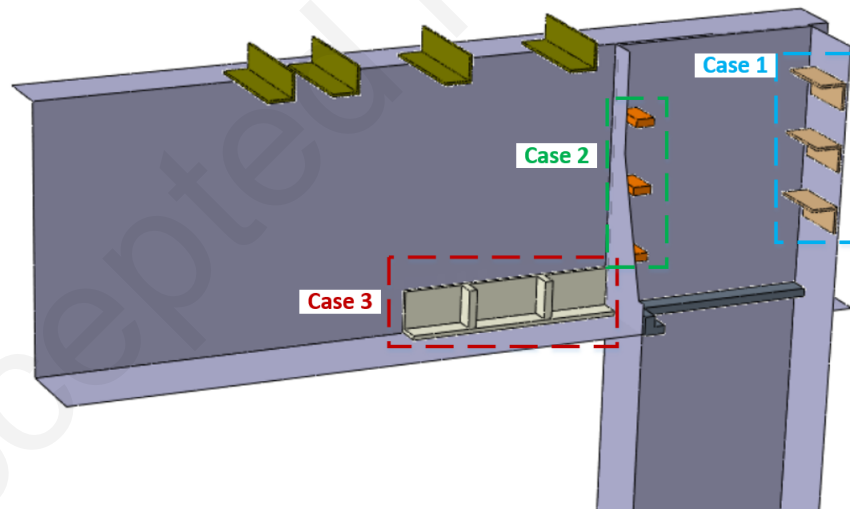


Figure 41: Cases for the parametric study

439

440 possible modifications. The following three cases are investigated (Fig. 41):

- 441 • For case 1, the L-angles (component ② in Fig. 6) that are welded to the outer flange of the
 442 column are replaced by 3 shear headed studs with a diameter of 19 mm and a length of 75

443 mm in order to avoid the concrete cracking presented in Fig. 28a.

444 • In case 2, steel pieces (component ⑤ in Fig. 6) that are welded to the inner flange of the
445 column are removed.

446 • In case 3, four of 8 steel pieces (component ③ in Fig. 6), two at each side, are removed.

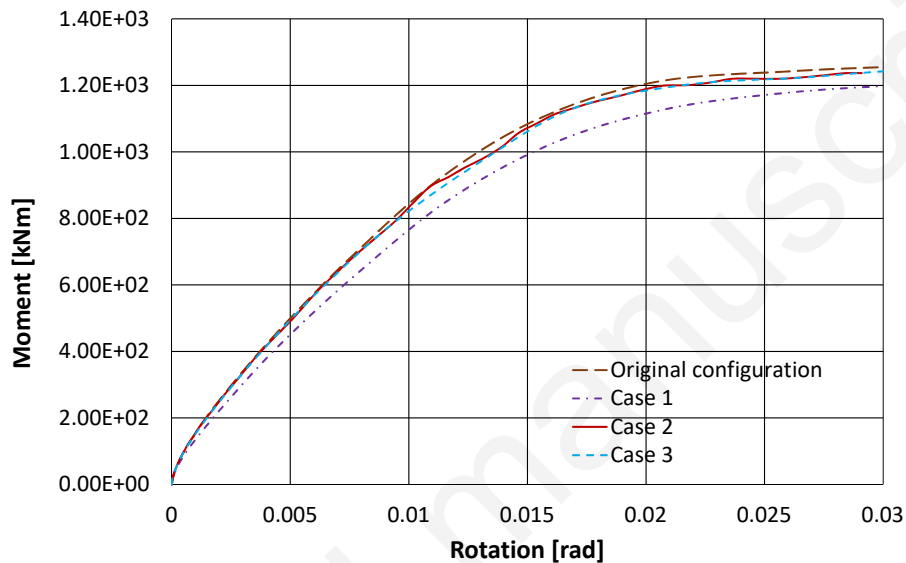


Figure 42: A comparison of moment-rotation curves for different cases of study.

447 Fig. 42 shows a comparison of the moment-rotation curves for the different cases of the study.
448 It is observed that the global behaviour of the joint changes only slightly for cases 2 and 3. Conse-
449 quently, component ③ may be simplified and component ⑤ could be removed. However, in case
450 1, the stiffness as well as the ultimate bending moment are significantly smaller than those in the
451 case of the initial configuration with L-angles. The numerical simulation therefore suggests that
452 the headed shear studs are less efficient than the L-angles in transferring the forces from the HA20
453 rebars to the exterior flange of the steel column. However, these conclusions should be considered
454 with caution, and experimental validation is needed.

455 6. Conclusion

456 This paper presents a study on the behaviour of the joint between a concrete-filled steel tubular
457 column and a U-shaped steel concrete beam. Two full-scale experimental tests of the joint have

458 been carried out in order to determine the moment resisting capacity, the deformation capacity,
459 the cracking patterns, and the failure mode of the joint. In order to obtain the understanding
460 of the load-transfer mechanism between the steel and concrete parts of the joint, a detailed FE
461 simulation of the joint has also been performed in ABAQUS/Explicit and validated against the
462 experimental data. On the basis of the result of the simulation, a practical design method has been
463 developed using the strut-and-tie model for concrete part and shear panel model for the steel part
464 of the joint, while taking into account a comprehensive load-transfer mechanism between the two
465 parts. From this study, the following outcomes can be extracted:

- 466 – The test results show that the failure mode of the studied configuration of the joint specimen
467 was governed by the buckling of the compressive flange of the column tube close to the joint.
468 This indicates that the strong column - weak beam criterion was not followed. However,
469 the design of the tested joint is adequate as the joint has sufficient stiffness for service loads
470 and high ductility at failure for ultimate loads. Based on EN1993-1-8, the tested joint is
471 semi-rigid, ductile, and fully resistant.
- 472 – The FE simulation of the test has been successfully performed and well validated against
473 the experimental observations. The result of the FE simulation match with most of the
474 phenomena observed in the experiment such as the cracking pattern of the damaged specimen,
475 the buckling of the compressive flange of the column tube, the crushing of the concrete at the
476 zone of buckled flange of the column tube, and the yielding zone of the steel tube as well as
477 of the U-shaped steel profile. The global behaviours of the joint such as the moment-rotation
478 curves and the distribution of slips and uplifts obtained from the simulation also agree well
479 with the ones obtained from the experiment.
- 480 – The design model of the joint includes the sophisticated load-transfer mechanism between the
481 steel and the concrete parts of the joint deduced from the FE simulation. For the concrete
482 model of the joint, the geometry of the strut-and-tie model was not chosen based on opinions,
483 but deduced from the stress map obtained from the simulation. The shear panel model of the
484 steel part consists of two sub-panels for equilibrium. Furthermore, the flanges and portions
485 of webs close to them are considered to handle the axial stresses. The validity of the design
486 model can be assessed by the confirmation of the yielding of the steel beam and the steel

487 column in the steel model of the joint as well as the yielding of the ties (rebars) in the concrete
488 model of the joint, which are the observations found in the numerical simulation. From these
489 validations, one can conclude that the classical strut-and-tie method remains applicable for
490 the concrete part of the joint, that the shear panel model stands pertinent for the steel part
491 of the joint, and that it is possible to combine the two models for the composite joint using
492 an appropriate load-transfer mechanism.

493 – The parametric study of the FE simulation demonstrates that the detail of the steel stiffeners
494 placed inside the joint to transfer the forces can be optimised.

495 In the future, it is interesting to confirm the result of the parametric study by performing exper-
496 imental tests on the optimised configurations of the joint. Furthermore, the current configuration
497 of the joint can be improved to follow the strong column-weak beam criterion, for tall structures
498 under seismic loading. In such a case, it is interesting to conduct further experimental tests using
499 reversed cyclic loading to investigate the cyclic behaviour of the joint.

500 **Acknowledgements**

501 The authors gratefully acknowledge financial support by the ANR (Agence Nationale de la
502 Recherche) and INGENOVA through the Labcom ANR B-HYBRID project.

503 **References**

- 504 [1] R. G. Slutter, G. C. Driscoll Jr, Flexural strength of steel-concrete composite beams, *Journal of Structural*
505 *Division* 91 (1965) 71–99.
- 506 [2] J. Nie, Y. Xiao, L. Chen, Experimental studies on shear strength of steel–concrete composite beams, *Journal*
507 *of Structural Engineering* 130 (2004) 1206–1213.
- 508 [3] H. Nordin, T. B., Testing of hybrid frp composite beams in bending, *Composites: Part B* 35 (2004) 27–33.
- 509 [4] J. Deng, M. K. Lee, S. Li, Flexural strength of steel–concrete composite beams reinforced with a prestressed
510 cfrp plate, *Construction and Building Materials* 25 (2011) 379–384.
- 511 [5] M. Shariati, N. R. Sulong, M. Suhatri, A. Shariati, M. A. Khanouki, H. Sinaei, Behaviour of c-shaped angle
512 shear connectors under monotonic and fully reversed cyclic loading: An experimental study, *Materials and*
513 *Design* 41 (2012) 67–73.
- 514 [6] M. Shariati, N. R. Sulong, A. Shariati, M. A. Khanouki, Behavior of v-shaped angle shear connectors: experi-
515 mental and parametric study, *Materials and Structures* 49 (2016) 3909–3926.

- 516 [7] M. Shariati, F. Tahmasbi, P. Mehrabi, A. Bahadori, A. Toghrol, Monotonic behavior of c and l shaped angle
517 shear connectors within steel-concrete composite beams: an experimental investigation, *Steel and Composite*
518 *Structures* 35 (2020) 237–247.
- 519 [8] C. C. Weng, S. I. Yen, M. H. Jiang, Experimental study on shear splitting failure of full-scale composite concrete
520 encased steel beams, *Journal of Structural Engineering* 128 (2002) 1186–1194.
- 521 [9] M. N. S. Hadi, J. S. Yuan, Experimental investigation of composite beams reinforced with gfrp i-beam and steel
522 bars, *Construction and Building Materials* 144 (2017) 462–474.
- 523 [10] M. M. Rana, C. K. Lee, S. AlDeen, Y. X. Zhang, Flexural behaviour of steel composite beams encased by
524 engineered cementitious composites, *Journal of Constructional Steel Research* 143 (2018) 279–290.
- 525 [11] K. W. Hoe, M. Ramli, Indicative performance of fiber reinforced polymer *frp* encased beam in flexure, *Con-*
526 *struction and Building Materials* 143 (2013) 279–290.
- 527 [12] D. J. Oehlers, Composite profiled beams, *Journal of Structural Engineering* 119 (1993) 1085–1100.
- 528 [13] B. Uy, M. A. Bradford, Ductility of profiled composite beams: Part i experimental study, *Journal of Structural*
529 *Engineering* 121 (1995) 876–882.
- 530 [14] S. Nakamura, Bending behaviour of composite girders with cold formed steel u section, *Journal of Structural*
531 *Engineering* 128 (2002) 1169–1176.
- 532 [15] Y. Liu, L. Guo, B. Qu, S. Zang, Experimental investigation on the flexural behaviour of steel concrete composite
533 beams with u-shaped steel girders and angle connectors, *Engineering Structures* 131 (2017) 492–502.
- 534 [16] L.-H. Chen, S.-T. Li, H.-Y. Zhang, X.-F. Wu, Experimental study on mechanical performance of checkered
535 steel-encased concrete composite beam, *Journal of Constructional Steel Research* 143 (2018) 223–232.
- 536 [17] P. Keo, C. Lepourry, H. Somja, F. Palas, Behaviour of a new shear connector for u-shaped steel-concrete hybrid
537 beams, *Journal of Constructional Steel Research* 145 (2018) 153–166.
- 538 [18] C. Lepourry, P. Heng, H. Somja, N. Boissonnade, F. Palas, An innovative concrete-steel structural system for
539 long-span structure allowing a fast and simple erection., *Structures (Article in press)* (2019).
- 540 [19] EN 1992, Eurocode 2: Design of concrete structures, European Committee for Standardization, 2006.
- 541 [20] EN 1993-1-8, Eurocode 3: Design of steel structures: Part 1-8: Design of joints, European Committee for
542 Standardization, 2005.
- 543 [21] EN 1994, Eurocode 4: Design of composite steel and concrete structures, European Committee for Standard-
544 ization, 2005.
- 545 [22] J. P. Jaspart, K. Weynand, Design of joints in steel and composite structures, ECCS Press and Wiley, 2016.
- 546 [23] A. Azizinamini, Y. Shekar, M. AlaSaadeghvaziri, Design of through beam connection detail for circular com-
547 posite columns, *Engineering Structures* 17 (1995) 209–213.
- 548 [24] T. M. Sheikh, G. G. Deierlein, J. A. Yura, J. O. Jirsa, Beam-column moment connections for composite frames:
549 part 1, *Journal of Structural Engineering* 115 (1989) 2858–2876.
- 550 [25] Z. Tsoa, W. Lib, B.-L. Shic, L.-H. Han, Behaviour of bolted end-plate connections to concrete-filled steel
551 columns, *Journal of Constructional steel Research* 134 (2017) 194–208.
- 552 [26] J. Fan, Q. Li, J. Nie, H. Zhou, Experimental study on the seismic performance of 3d joints between concrete-filled
553 square steel tubular columns and composite beams, *Journal of Structural Engineering* 140 (2014) 04014094.

- 554 [27] H.-G. Park, H.-J. Hwang, C.-H. Lee, C.-H. Park, C.-N. Lee, Cyclic loading test for concrete-filled u-shaped steel
555 beam-rc column connections, *Engineering Structures* 36 (2012) 325–336.
- 556 [28] H.-J. Hwang, T.-S. Eom, H.-G. Park, S.-H. Lee, H.-S. Kim, Cyclic loading test for beam-column connections of
557 concrete-filled u-shaped steel beams and concrete-encased steel angle columns, *Journal of Structural Engineering*
558 141 (2015) 04015020.
- 559 [29] Abaqus documentation, version 6.14., Dassault system (2014).
- 560 [30] NF EN12390-3, Testing harden concrete: Compressive Strength of Test Specimens, AFNOR - French standard
561 institute, 2003.
- 562 [31] NF EN ISO 6892-1, Metallic materials - Tensile testing - Part 1 : method of test at room temperature, AFNOR
563 - French standard institute, 2009.
- 564 [32] Aramis v8 manual basic, GOM mbH, Braunschweig (2015).
- 565 [33] B. Alfarah, F. López-Almansa, S. Oller, New methodology for calculating damage variables evolution in plastic
566 damage model for rc structure, *Engineering structures* 132 (2017) 70–86.
- 567 [34] C. Lepourry, Behaviour of U-shaped Steel Concrete Hybrid Beam, PhD dissertation, INSA Rennes, 2019.
- 568 [35] G. Loho, A. Lachal, Modelling of strengthened column web panel in bolted end-plate composite joints, *Journal*
569 *of Constructional Steel Research* 64 (2008) 584–595.
- 570 [36] B. Mou, Y. Bai, Experimental investigation on shear behavior of steel beam-to-cfst column connections with
571 irregular panel zone, *Engineering Structures* 168 (2018) 487–504.
- 572 [37] B. Mou, L. Pang, Q. Qiao, Y. Yang, Experimental investigation of unequal-depth-beam-to-column joints with
573 t-shape connector, *Engineering Structures* 174 (2018) 663–674.

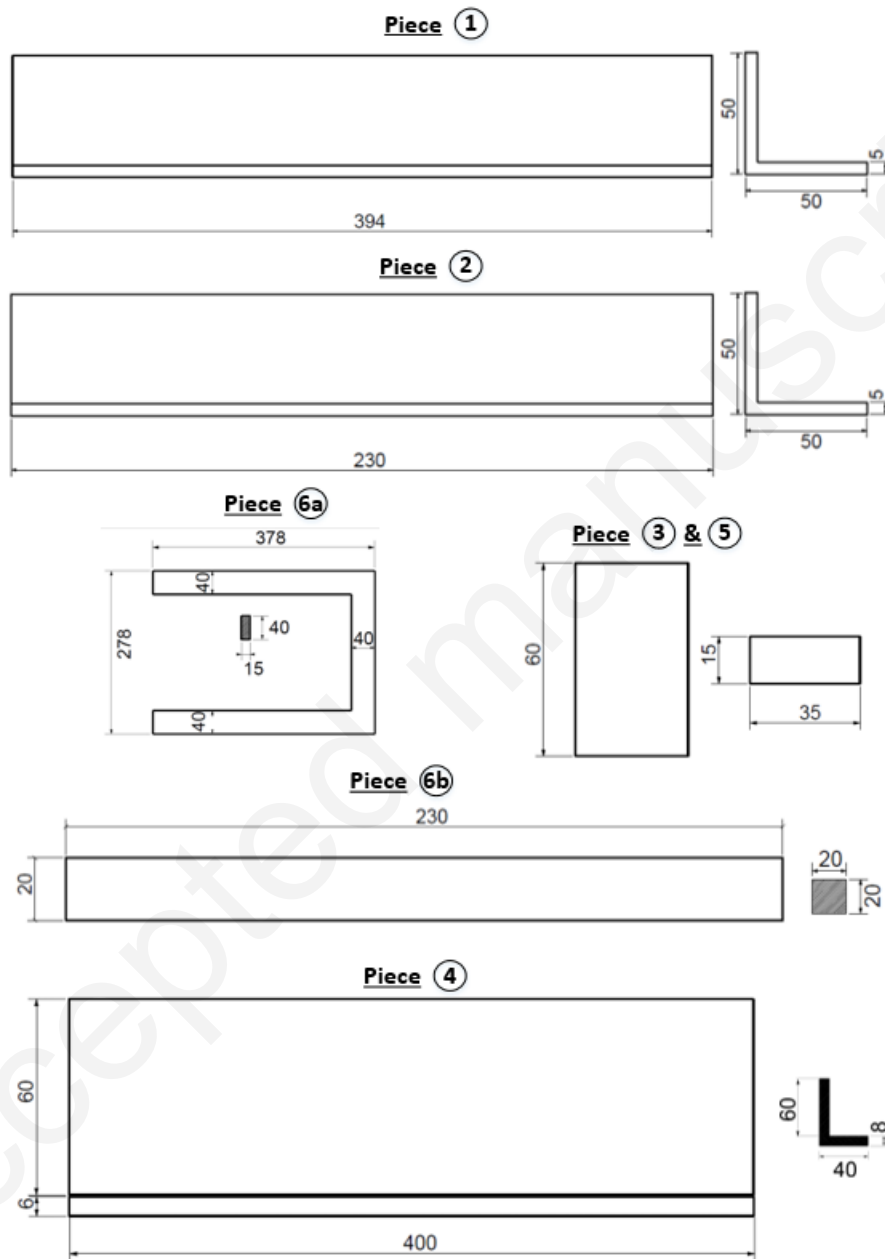


Figure 44: Dimensions of steel pieces.

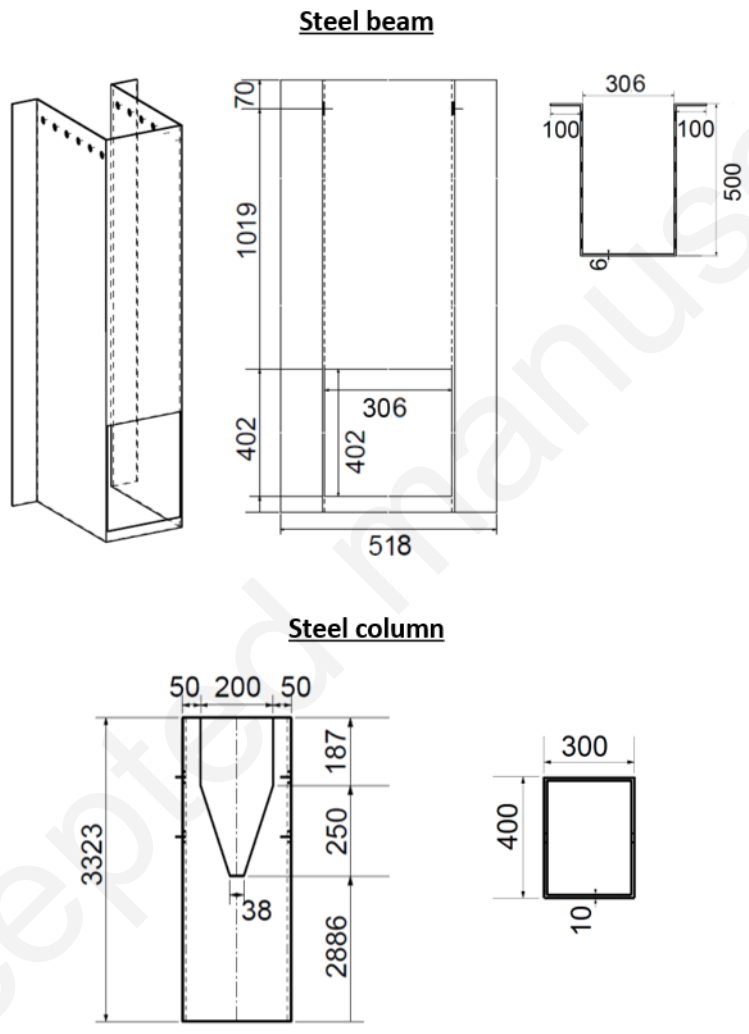


Figure 45: Detail of steel beam and steel column.

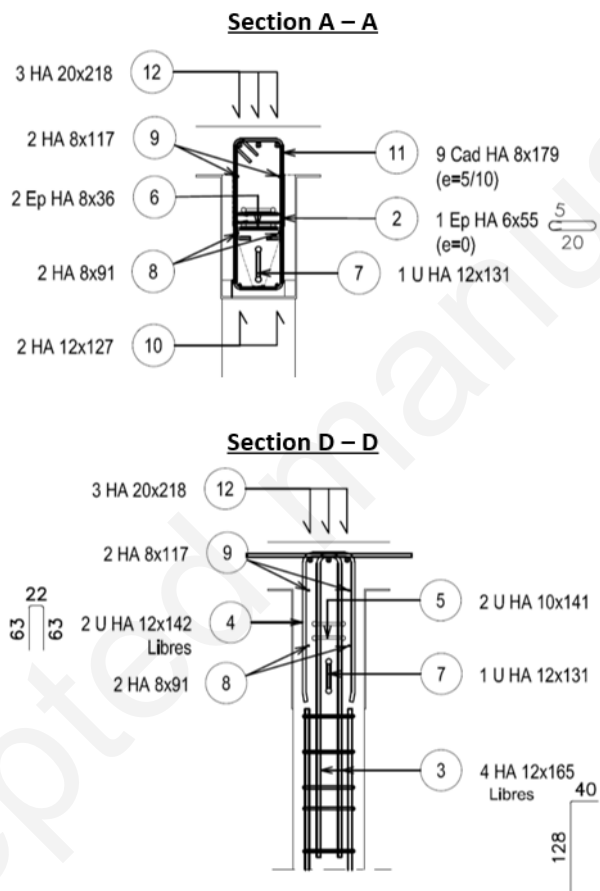


Figure 47: Details of sections.